Delft University of Technology

Department of Materials Science and Engineering

Faculty of Mechanical, Maritime and Materials Engineering

Data-Driven Material Characterisation of Multicomponent Atherosclerotic Arteries

---

A thesis submitted in partial fulfilment of the requirements
for the degree of Master of Science in

Materials Science and Engineering

To be defended on 11th May 2023 at 09:00

Author
Lucy Seager
5363411

Graduation Committee
Dr. S. Kumar (supervisor)
Dr. A.C. Akyildiz (supervisor)
Dr. M.P. Peirlinck

Abstract

Cardiovascular diseases continue to be the primary cause of death worldwide, where the buildup of plaque within arterial walls, known as atherosclerosis, is a major contributor to various acute cardiovascular events. Determining the material properties and the resulting stress distributions is crucial in the risk assessment of atherosclerotic plaques, as stress is considered an indicator of plaque vulnerability. Material models can be found with stress-strain pairs, but experimentally determining stress tensors is challenging. To address this limitation, we use a recently developed technique called EUCLID (Efficient Unsupervised Constitutive Law Identification and Discovery) for material characterisation of a two-dimensional multicomponent atherosclerotic plaque, based solely on displacement and force data. A finite element model was developed to simulate the mechanical behaviour of the plaque using the neo-Hookean hyperelastic model, and noisy data was introduced into the model by applying Gaussian noise on the displacements. An L-BFGS gradient descent optimiser was used to minimise the objective function, which is the residual error between predicted internal forces and true external forces. Results showed that at the expected noise level in clinical imaging modalities, no physically relevant stress distributions were obtained, where the plaque's heterogeneity was observed to affect the accuracy. Clinical imaging was further emulated by systematically removing data to determine the effect of missing data on the model. No significant deterioration of the accuracy of obtained parameters was seen until using 10% of the total data, indicating good robustness to missing data. While the study has limitations, the proposed approach could have implications for the future diagnosis and treatment of atherosclerosis. Future research could explore alternative optimisation algorithms or techniques to improve the model's accuracy under these conditions.

Contents

Declaration

I hereby declare that except where specific reference is made to the work of others, the contents of this thesis are original and have not been submitted in whole or in part for consideration for any other degree or qualification in this, or any other university. This thesis is my own work and contains nothing which is the outcome of work done in collaboration with others, except as specified in the text and Acknowledgements.

Lucy Seager
May 2023

Acknowledgements

A year ago I jumped into the deep end of this project with very little prior knowledge on the topic, and although it came with its challenges, I've learnt more than I could have ever imagined, and for that alone I am incredibly grateful. It would not have been possible without a few people in particular, so I would like to begin this thesis by saying thank you to them for their helping hand along the way.

First and foremost, my supervisors - Dr. Sid Kumar and Dr. Ali Akyildiz. Sid's unwavering support was invaluable, especially his thorough explanations of everything from continuum mechanics to the EUCLID framework, as well as his patience with me when the programming learning curve was particularly steep. I am also indebted to Ali from Biomechanical Engineering. His expertise in atherosclerosis and biomechanics was indispensable in helping me understand the complex mechanisms underlying the disease, both during the literature research and project phase. Their guidance and passion for the subject were instrumental in shaping my understanding and knowledge of the topic, and their support throughout the project was greatly appreciated.

It's been an honour to be part of the MMC group, which has given me the opportunity to work with some exceptional minds in the field. Notably, Akshay, who provided invaluable support in the early stages of the project. I am very grateful for his enthusiasm and encouragement, even from afar. Additionally, thank you to Prakash for his help in weekly meetings and setting me up with the necessary computational tools right from the get go.

Also, a massive thanks to my Delft family - Eider, Jelle, Maria, Karthik and Thom for their friendship and moral support. Our coffees and lunches were always a welcomed break from work and I feel very lucky to call you guys my friends.

And last, but definitely not least, my loving parents, Jo and Ashley, and my sister Emily, for their ongoing encouragement and belief in me throughout my whole academic journey. I am especially grateful for all the sacrifices my parents have made over the years to make my dreams a reality.

1 Introduction

Cardiovascular diseases remain the primary cause of mortality, accounting for over 18 million deaths globally in 2021 (1). Hereditary factors, obesity, and high cholesterol are among the key contributors to the onset of these diseases, which impose a substantial burden on patients' health and healthcare systems. Atherosclerosis, characterised by the accumulation of fatty and/or fibrous material in the intima of arteries, triggers the development of cardiovascular diseases, and is further associated with stenosis (arterial narrowing) and the potential for thrombosis following plaque rupture (2). Accurate prediction of plaque rupture is a challenging task that necessitates an in-depth understanding of the underlying mechanisms governing plaque growth and failure, as well as sophisticated tools and techniques for identifying vulnerable plaques. Despite an established classification system for vulnerable plaques, significant challenges persist in developing predictive models that are sufficiently precise in assessing the likelihood of plaque rupture.

The assessment of plaque rupture risk is of significant importance in clinical practice, and given the patient-specific nature of plaque morphology, there is a pressing need for non-invasive tools to facilitate this evaluation. To accurately characterise plaque vulnerability, information regarding the stress distribution within the plaque is required. However, while clinical imaging modalities can provide valuable displacement data, they do not provide direct stress information. A potential avenue for addressing this challenge lies in utilising blood pressure measurements, in conjunction with the aforementioned displacement data, to develop a risk assessment technique that could prove effective in the absence of direct stress data. Therefore, in this study we aim to explore the potential use of a simplified EUCLID (Efficient Unsupervised Constitutive Law Identification and Discovery)(3) framework in characterising the material properties of atherosclerotic plaques, based only on full-field displacement data and static equilibrium assumptions. Specifically, we investigate the neo-Hookean material parameters of a two-dimensional (2D) heterogeneous atherosclerotic plaque at the expected noise level in intravascular ultrasound (IVUS).

This work is structured as follows: we begin with an overview of EUCLID and atherosclerosis; then we present the finite element model used to simulate the mechanical behaviour of the plaque to obtain full-field displacement data, using the neo-Hookean hyperelastic material model. We discuss the techniques and constraints used to discretise the model and solve the resulting linear system of equations using the Limited-memory Broyden–Fletcher–Goldfarb–Shanno algorithm (L-BFGS). Finally, we examine the implications of our results for the diagnosis and treatment of atherosclerosis. Overall, the study demonstrates that the EUCLID framework and L-BFGS optimisation implemented in this study still need improvement for determining the material parameters of atherosclerotic plaques at the expected noise level in IVUS; however, future research may explore alternative modelling approaches or optimisation techniques to improve accuracy in obtaining material parameters and enable more reliable predictions of plaque rupture.

1.1 EUCLID

EUCLID is a data-driven technique developed by Kumar *et al.*, which allows for the discovery of parsimonious constitutive laws for isotropic hyperelastic materials (3). It does so without stress data and with only displacement and force data. The lack of stress data is circumvented by enforcing linear momentum balance, as discussed in more depth in subsection 2.2. In the presence of noisy displacement data, it automatically discovers constitutive models using sparse regression on a large feature library. The feature library is comprised of three parts: polynomial hyperelasticity laws (Mooney-Rivlin); volumetric deformation features; and logarithmic features (Gent and Thomas). In this work we use a simplified form of the EUCLID framework which does not depend on a feature library as only the neo-Hookean hyperelastic constitutive model is used, however, the underlying concepts of linear momentum balance and the resulting linear system of equations remains the same as the original framework.

To date, EUCLID has been used on hyperelastic materials (3) and has also been extended for path-dependent elastoplasticity to discover hardening mechanisms (4), as well as for neural network (NN) training for hyperelastic materials (5). The NN method is similar to the approach in (3), but it is extended to learn several anisotropic constitutive models as well, where accurate estimates of the fibre orientations were found, even in cases of high noise. The NN-based models were also shown to be capable of predicting different material behaviour, even in cases which are different to those which the models were trained on. Good accuracy was achieved, even on simulations with complex boundary conditions. In the case where EUCLID is applied to plasticity, the material model library is created from a Fourier series expansion of a yield function, where EUCLID selects the best Fourier mode based on a balance of linear momentum and from this the hardening behaviour can be determined. Accurate results were obtained for different types of plastic yield surfaces and hardening mechanisms (4). Additionally, the EUCLID framework has been extended to include Bayesian learning in order to discover elastostatic and elastodynamic isotropic and anisotropic hyperelastic models. The Bayesian learning approach allows EUCLID to estimate posterior probabilities based on displacements, accelerations, reaction forces and the conservation of linear momentum, and from this the material models are given via probability distributions. This Bayesian-learning approach improved the speed and efficiency of data usage by two orders of magnitude compared to previous uses of EUCLID with hyperelastic materials (6).

1.2 Atherosclerosis

Atherosclerosis is a chronic inflammatory disease characterised by the buildup of substances such as fats and cholesterol in the inner lining of arteries, leading to narrowing and hardening of blood vessels, particularly carotid, iliac and aortic arteries. The narrowing of arteries increases the risk of heart attack, stroke and other acute cardiovascular complications, since a ruptured plaque can block the flow of blood and consequently can trigger a thrombotic event. Risk factors for atherosclerosis include high blood pressure, smoking, obesity, diabetes, high cholesterol levels and a sedentary lifestyle, which can all contribute to endothelial dysfunction and plaque development.

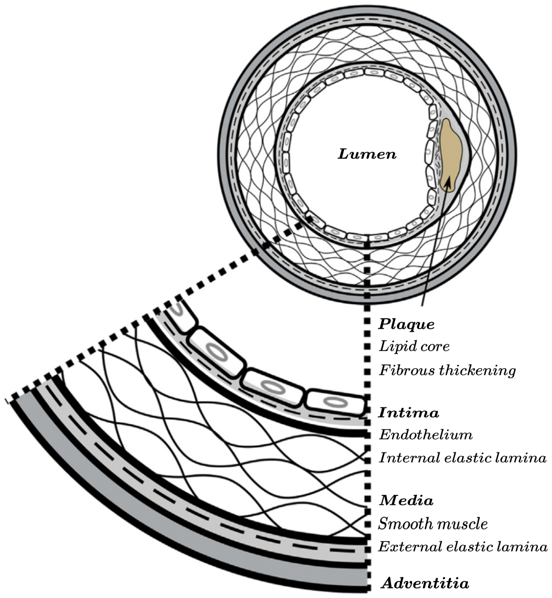

Figure 1: *Cross section of an artery with atherosclerosis. Adapted from* (7)

As shown in Figure 1, the three components of the blood vessel (intima, media and adventitia) form three concentric layers (7). The innermost layer (intima) forms the interface with the lumen via a single layer of endothelial cells, which regulates transfers between the blood vessel and tissue. It is this layer which is predominantly affected by atherosclerosis. The vascular smooth muscle cells (VSMCs) in the media are separated from the intima by the internal elastic lamina, where the migration of VSMCs to the intima is associated with the pathogenesis of atherosclerotic plaques (8). The fibrous cap refers to the region of the intima which separates the lipid-rich plaque core from the lumen, but evolves from the original intima tissue due to the VSMCs which enter the sub-endothelial layer. During atherosclerosis, the endothelial layer becomes damaged and inflammatory cells migrate into this region. The VSMCs play a role in plaque development and stabilisation by synthesising extracellular matrix components, such as collagen and elastin, which contribute to the fibrous cap (9). Additionally, foam cells form when macrophages, a type of white blood cell, engulf oxidized low-density lipoprotein (LDL) particles. These foam cells accumulate in the intima layer and contribute to the development of the "fatty streak" in the earliest stages of disease development, which subsequently forms the atheroma, characterised by a significant growth of the lipid-rich plaque core (10). It should be noted, however, that while VSMCs contribute to the formation of the plaque, their presence in the fibrous cap is beneficial for plaque stability, since thinning of the cap is partly due to a reduction in VSMCs, which in turn reduces collagen production (11).

The presence of calcified tissue within the intima also indicates a more advanced, and potentially vulnerable, atherosclerotic plaque. The amount of calcification depends on the patient's disease progression, but it affects the overall mechanical behaviour since the strength and stresses of a plaque depend on the composition. This tissue is the stiffest of the plaque components and numerous studies report a Young's modulus value in the range of GPa; the same as cortical bone. This is due to the expression of bone regulating proteins and bone-like cells during the formation of calcifications (12). Furthermore, calcium is a major component of calcified tissue, forming calcium phosphate crystals such as hydroxyapatite, which contribute to the hardening of the plaque. These crystals form microcalcifications, and as an atheroma develops, clusters of them coalesce and form larger, unified macrocalcifications. Additionally, calcified tissue can in some cases stabilise the plaque and make it less prone to rupture, but it can also make the plaque more brittle and increase the risk of fracturing (13).

Plaque vulnerability is attributed to a series of morphological and compositional features that make them more prone to rupture, but typically it is characterised by a thin or fragmented and inflamed fibrous cap overlying a large lipid-rich necrotic core, where necrotic refers to dead or devitalised tissue (14). The fibrous cap becomes thin and vulnerable to rupture particularly in regions where there is increased stress due to either hydrostatic blood pressure, shear blood flow or circumferential stress generated by the wall (15). Plaque rupture is a complex biological event but ultimately occurs when the stresses on the fibrous cap exceed the local strength of the tissue (12). The peak cap stress of the fibrous cap is therefore of particular importance. This is defined as the maximum stress the fibrous cap can withstand before it ruptures, where the value depends on the properties of the cap, such as thickness and stiffness. As the atherosclerotic plaque grows and the fibrous cap becomes thinner and weaker, the peak cap stress increases since the cap is less able to withstand the forces exerted on it. Accurately predicting the stress distribution in atherosclerotic plaques can help to identify regions where the stress exceeds the peak cap stress, and is therefore more likely to cause rupture. This information can be used to better characterise plaque vulnerability and to guide earlier interventions aimed at stabilising vulnerable plaques, as well as potentially preventing adverse cardiovascular events.

Imaging modalities can be used to identify features of a vulnerable plaque; however, the characterisation of atherosclerotic plaque presents significant challenges due to variations in plaque vulnerability, as well as the tissue's inherent heterogeneity. Although there is agreement regarding the stiffness of certain regions, stiffness values vary significantly between studies. Furthermore, there have been reports of plaques rupturing despite being deemed low-risk based on these criteria (16), highlighting the need for more accurate and reliable predictors of plaque vulnerability.

Studies on the material characterisation of atherosclerotic plaques are typically conducted *ex vivo*, but there is a scarcity of human specimens, resulting in testing often being performed using pig or other animal arteries. The values obtained from these studies exhibit significant variability between patients and across different studies, which can be attributed to differences in plaque location, plaque age, and gender. Additionally, the direction of plaque cutting can impact the mechanical behaviour of the plaque during testing. Furthermore, the type of mechanical testing, such as indentation or inflation testing, which produce local or global stiffness measurements, respectively, lead to discrepancies in results.

2 Method

2.1 Finite Element Modelling

2.1.1 Geometry

Figure 2 shows the 2D heterogeneous geometry of the cross-section used in this study, created from histology images of a carotid arteries (17). Within each of the four domains, the material is considered homogeneous. The geometry is discretised into a finite triangular element mesh with 16,352 nodes. The outer diameter is approximately 10 mm and the lumen diameter is approximately 3 mm. Based on the ground truth values presented in Table 1, an increase in intraluminal pressure from 80 to 120 mmHg (corresponding to a change in pressure from 10.64 to 15.96 kPa) results in a 10.9% increase in lumen area, which is consistent with values found in literature (18)(19). Displacements are generated under a plane strain assumption, which is the assumption that loads are applied to a three-dimensional body such that deformation occurs in two dimensions only, and the third dimension is prevented from deforming. This is valid in this work as we assume negligible deformation in the longitudinal direction of the artery, due to radially applied pressure.

2.1.2 Displacement Data Generation

The Finite Element Method (FEM) is a numerical technique which simplifies problems in applications such as structural analysis, heat transfer, fluid mechanics, electromagnetics and acoustics by discretising a continuum into finite elements. Each element can be analysed separately since it is difficult, or even impossible, to solve problems analytically across a whole continuum. In this work, the elements are chosen to be triangular, where each element is characterised by three nodes and their respective shape functions. Triangular elements provide more geometrical flexibility due to the organic shape of the specimen, as shown in Figure 2, and require fewer nodes and degrees of freedom (DOFs), thus leading to higher computational efficiency. Shape functions are mathematical functions which allow us to interpolate displacements and deformations across the body. DOFs also define displacement and deformation within the body, but they specify the number of ways that a node can move or deform under external loads, i.e. in two dimensions each node has two DOFs.

The FEM is used in this work to generate the displacement fields required for the input of EUCLID, simulated on the specimen shown in Figure 2. Implemented in Python, the FEM uses the static equilibrium equation

$$\underline{\underline{K}}\,\underline{u} = \underline{f}\ , \tag{1}$$

to solve for displacements $\underline{u}$ at each degree of freedom, where $\underline{\underline{K}}$ is the tangent stiffness tensor and $\underline{f}$ is the vector containing the forces on each degree of freedom. The 2D geometry results in two-degrees of freedom per node. If one stable solution exists then $\underline{\underline{K}}$ is invertible and the full-field displacements are obtained from $\underline{u} = \underline{\underline{K}}^{-1}\underline{f}$.

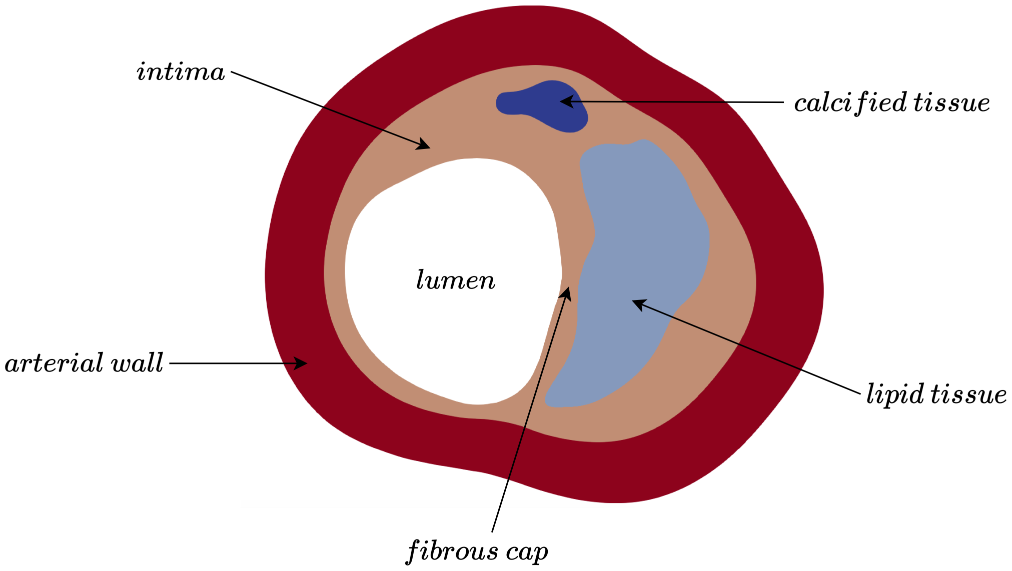

Figure 2: *Schematic of the 2D heterogeneous arterial wall, deformed by an intraluminal pressure of 120 mmHg (15.96 kPa). Regions displayed are the diseased tunica intima (intima), lipid-rich necrotic core (lipid tissue), calcified tissue, and the arterial wall, which is a combined form of the tunica media and tunica adventitia. The fibrous cap is part of the intima but is distinguished here as the region separating the lipid tissue from the lumen. Geometry from (17).*

The tangent stiffness matrix $\underline{\underline{K}}$ is constructed at each load step and requires the nodal coordinates (x, y) in the updated deformed configuration, and the stress and strain at each element's quadrature point. It represents the relationship between the applied forces and the resulting deformation. When modelling the material using linear elasticity, the tangent stiffness is equivalent to the stiffness matrix, and is therefore constant since it does not depend on the magnitude of the applied stress. However, this work uses the neo-Hookean hyperelastic model, where deviation from the linear stress-strain relationship is observed at higher strains. In this case $\underline{\underline{K}}$ represents the derivative of the stress with respect to the strain and is calculated using the material's constitutive law.

When displacement data for the neo-Hookean model is generated, a Newton-Raphson iterative procedure must be adopted, which uses successive linearisations of the strain due to the non-linearity. In order to find the successive displacement u_{i+1}, we perturb the system by Δu, such that $u_{i+1} = u_i + \Delta u$. The perturbation term can be rewritten as $\underline{\underline{K}}^{-1}\underline{f}$, since $\underline{\underline{K}}$ is a square, invertible matrix ($n_d \times n_d$ where n_d is the total number of degrees of freedom), and $\underline{f}$ represents the difference in internal and external forces. The solution must converge to a residual as close to zero as possible, and in the case where the residual is not sufficiently small then the process is repeated until the norm of all forces is below 10^{-8}.

2.1.3 Dirichlet Boundary Conditions

Dirichlet boundary conditions specify the value that a solution to a differential equation should take at a boundary, thus we use them to impose null displacements on three degrees of freedom at each load step, such that the artery is free to expand radially but has sufficiently constrained rigid body motion. The three degrees of freedom correspond to rotational and translation motion in the $x-y$ plane. In order to preserve the natural radial expansion, the three degrees of freedom, belonging to two nodes, were chosen using the maximum and minimum x coordinates of all nodes, as portrayed in Figure 3. This allowed the lumen nodes to move freely, giving accurate displacements here and inside the artery, as well as avoiding non-convergence caused by infinite possible displacements and thus a high force residual. In this case the finite element model would not be able to find a stable solution.

2.1.4 Neumann Boundary Conditions

Neumann boundary conditions prescribe the normal derivative of a differential equation and are therefore used here to prescribe a traction on the lumen nodes. Traction is a vector quantity which represents the force per unit area acting on a surface and has normal and tangential components. The two-dimensional geometry used in this work requires the traction to be applied on an edge between two neighbouring nodes on the lumen boundary, which therefore represents the force per unit edge length. The force arises from the blood pressure exerted on the inner wall of the artery. Since Neumann boundary conditions specify normal derivatives, we consider the normal component of the traction vector on the lumen boundary as the Neumann boundary condition. The force $\underline{f}$ acting on node a is modelled as the relative contribution of edge forces from the edges either side of it, i.e.,

$$\underline{f}^a = \frac{1}{2}Pl_1\underline{n}_1 + \frac{1}{2}Pl_2\underline{n}_2\ , \tag{2}$$

where P is the blood pressure, l is the distance of the edge between two nodes and

$\underline{n}$ is the normal vector of the edge, as displayed in Figure 3. This traction emulates the force generated with every heartbeat as blood is pumped through blood vessels, which ranges from the diastolic pressure ($\approx$ 80 mmHg) to the systolic pressure ($\approx$ 120 mmHg), where 10 mmHg = 1.33 kPa. The pressure is assumed to be static (i.e. no pulsatility) and P = 120 mmHg was used to model the material behaviour since the highest risk for plaque rupture is seen with an elevated blood pressure (20).

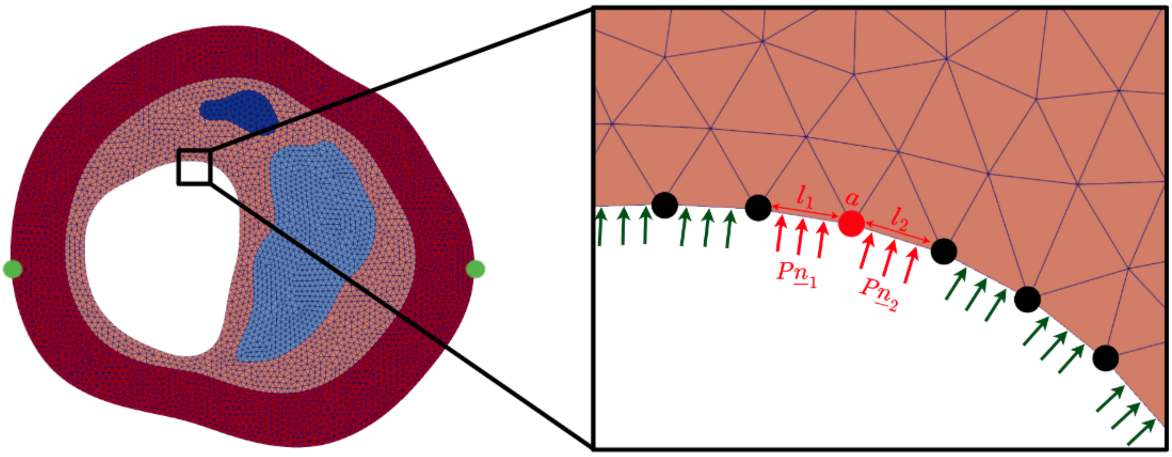

Figure 3: *Schematic of the finite element mesh with Dirichlet and Neumann boundary conditions. Neumann boundary conditions are imposed on all degrees of freedom which lie on the lumen boundary to emulate intraluminal blood pressure. The black dots denote the lumen nodes where traction is applied. The components of Equation 2 are highlighted in red. The green dots on the wall edge represent the positions where Dirichlet boundary conditions are imposed to fix three degrees of freedom, whereby all displacement is constrained to zero.*

The pressure is constrained to act only in the outward normal direction, i.e. away from the lumen centre, by implementing a check such that the vector from the midpoint between two nodes to the third lumen element (not on the lumen boundary), with the normal vector must be positive.

2.1.5 Clinical Imaging and Noise

Clinical imaging modalities, such as IVUS or magnetic resonance imaging, provide plaque data directly from patients, from which we can obtain displacement data. However, displacement data inherently contains noise which degrades the quality of measurements. Noise is caused by a variety of factors, but is mainly due to electronic noise in the measurement system, as well as physical vibrations or movements of the specimen. In order to emulate clinical imaging conditions, noise is added to each material point by means of Gaussian noise, which is defined via its mean and standard deviation σ. To this end, noisy displacement data is generated with a mean of 0 and

$\sigma = [10^{-10}, 10^{-9}, 10^{-8}, 10^{-7}, 10^{-6}, 10^{-5}, 10^{-4}, 10^{-3}]$, defined in units of mm. The use of multiple noise levels allows close examination of the performance of evaluating material parameters with EUCLID. According to Lee *et al.* (21), the expected noise level in the axial direction of IVUS is 1 μm (10^{-3} mm), where the ultrasound axial direction is parallel to the ultrasonic waves, but perpendicular to the 2D body used in this study. This noise level serves as a threshold for evaluating the accuracy of the C_{10} parameters obtained.

2.2 EUCLID

2.2.1 Displacement Fields

We define a as the global node number and u_i^a as the nodal displacement, where $i = \{1, 2\}$ denotes the degree of freedom. The displacement field is

$$u_i(\underline{x}) = \sum_{a=1}^{n_n} u_i^a N^a(\underline{x}) \ , \tag{3}$$

where n_n is the total number of nodes and $N^a(x)$ the shape function, such that $N^a(x) = 1$ when $x = x^a$ and $N^a(x) = 0$ when $a \neq b$, hence the displacement field $u_i(\underline{x})$ only includes contributions from node a and its respective shape function $N^a(\underline{x})$.

2.2.2 Deformation Fields and Hyperelasticity

The deformation gradient second-order tensor F_{ij} is defined as

$$F_{ij} = \frac{\partial x_i}{\partial X_j} \ , \tag{4}$$

where x_i denotes positions of particles in the deformed configuration and X_j are positions in the reference, or undeformed, configuration. F_{ij} describes how material points move in relation to neighbouring points when the specimen is subject to deformation and in three-dimensions contains nine quantities (22). Since we consider a two-dimensional material, the components of F_{ij} are F_{11}, F_{12}, F_{21} and F_{22}, where 1 and 2 denote the x and y directions, respectively.

We consider Equation 4 per element's quadrature point in the discretised mesh as

$$F_{ij} = \delta_{ij} + \sum_{a=1}^{n_n} u_i^a \frac{\partial N^a(\underline{x})}{\partial x_j} \ , \tag{5}$$

where δ_{ij} represents the Kronecker delta and accounts for the undeformed configuration.

Biological tissue exhibits a non-linear strain response as a result of stress due to an applied force, therefore the heterogeneous specimen is modelled as a neo-Hookean hyperelastic material. The neo-Hookean model represents stress through the first Piola-Kirchhoff stress tensor

$$P_{ij} = \frac{\partial W}{\partial F_{ij}} \ , \tag{6}$$

where W is the strain energy density function. The full form of this equation is shown in subsection A.3. We define the strain energy density as

$$W = C_{10}(\tilde{I}_1 - 3) + D_1(J - 1)^2 \ , \tag{7}$$

where $\tilde{I}_1$ is the deviatoric first invariant of the right Cauchy-Green deformation tensor. J is the Jacobian such that $J = \det(F_{ij})$, which represents the relative volume expansion produced by a deformation. The second Lamé parameter, μ, also known as the shear modulus, is related to C_{10} via $\mu = 2C_{10}$, and is assumed constant throughout deformation in the neo-Hookean model. The constant D_1 is related to the bulk modulus κ as $\kappa = 2/D_1$, and represents the amount of incompressibility in the material.

Values for the Young's modulus E of each domain are taken from literature and displayed in Table 1. We assume a known Poisson's ratio of $\nu = 0.49$ due to the approximate incompressibility of biological tissue, where ν represents the ratio of contraction or expansion in the direction perpendicular to the strain extension, which occurs in the direction of the applied force. From E we obtain domain-dependent C_{10} and D_1 values from

$$C_{10} = \frac{E}{4(1+\nu)} \ , \tag{8}$$

and

$$D_1 = \frac{6(1-2\nu)}{E} \ . \tag{9}$$

Tissue Type	**Young's Modulus (kPa)**	**C_{10} (kPa)**	**D_1 (kPa)**
Calcified	2300 (23)	386.0	5.22×10^{-5}
Lipid	18 (23)	3.02	6.67×10^{-3}
Intima	200 (24)	33.6	6.00×10^{-4}
Wall	90 (25)	15.1	1.33×10^{-3}

Table 1: *Ground truth values of the Young's modulus and the resulting neo-Hookean constants C_{10} and D_1 values for each tissue type in the multicomponent 2D body.*

2.2.3 Equilibrium

To circumvent the lack of stress data, we enforce the balance of linear momentum. In static equilibrium and assuming no body forces, the balance of linear momentum is

$$\nabla \cdot \boldsymbol{P} = 0 \;, \tag{10}$$

where $\boldsymbol{P}$ is the first Piola-Kirchhoff stress tensor. This is equivalent to saying that the residuals of the stress field must be zero across the whole body in static equilibrium, and can be rewritten as

$$\frac{\partial P_{ij}}{\partial X_j} = 0 \quad \forall \quad \underline{X} \;. \tag{11}$$

These equations impose the strong form, which says that the equilibrium condition from Equation 10 must be met at every point in the field, but this is a difficult condition to impose so instead we enforce it via the weak form, such that

$$\int V_i \frac{\partial P_{ij}}{\partial X_j} \, \mathrm{d}\underline{x} = 0 \tag{12}$$

where V_i is a vector-valued test function. This is the weak form because instead of the condition being met at all points, it says that the condition is met only in an average sense, at each element within a body, thus reducing the requirement for continuity on the test functions (shape functions).

In order to remove the divergence of the stress field from Equation 12 we integrate by parts and use Gauss' divergence theorem ($\int_V \nabla \cdot \underline{A} \, \mathrm{d}V = \int_S \underline{A} \cdot \underline{\hat{n}} \, \mathrm{d}S$, with $\underline{A}$ representing a vector field) to remove the remaining divergence of the product between P_{ij} and V_i to obtain

$$\int_{\Omega} P_{ij} \frac{\partial V_i}{\partial x_j} \, \mathrm{d}\underline{x} = \int_{d\Omega} P_{ij} V_i n_j \, \mathrm{d}\underline{x} \;. \tag{13}$$

The Bubnov-Galerkin method converts a continuous operator into a discrete problem, so this allows us to rewrite the test function as

$$V_i(\underline{x}) = \sum_a V_i^a N^a(\underline{x}) \;, \tag{14}$$

where $N^a(x)$ is the shape function of each node, such that $a \in \{1, 2, ..., n_n\}$ and n_n is the total number of nodes. V_i^a is an arbitrary weight of each shape function. We can then rewrite Equation 13:

$$\sum_a V_i^a \left(\int_\Omega P_{ij} \frac{\partial N^a(x)}{\partial x_j} \, \mathrm{d}\underline{x} - \int_{d\Omega} P_{ij} n_j N^a(x) \, \mathrm{d}\underline{x} \right) = 0 \; . \tag{15}$$

Since we have defined V_i^a to be an arbitrary weight, Equation 15 holds true for all V_i^a. We can use that $\sum_i c_i d_i = 0 \quad \forall \quad c$ implies that $d_i = 0$, since the summation must be zero for all c_i. Equation 15 therefore reduces to the following force balance equation between internal and boundary degrees of freedom

$$\int_\Omega P_{ij} \frac{\partial N^a(x)}{\partial x_j} \, \mathrm{d}\underline{x} - \int_{d\Omega} P_{ij} n_j N^a(x) \, \mathrm{d}\underline{x} = 0 \; , \tag{16}$$

where the first integral represents the internal forces due to the stresses within the finite element body, and the second integral represents the external forces due to the traction applied on the boundary nodes of the body.

2.2.4 Constraints

We define the degrees of freedom as $\mathcal{D} = \{a, i\}$, where $i \in \{1, 2\}$ in two dimensions. $\mathcal{D}$ is divided into two sets: $\mathcal{D}^{\text{free}}$ and $\mathcal{D}^{\text{lumen}}$. $\mathcal{D}^{\text{free}}$ contains all the degrees of freedom which do not have an external force applied directly on them, i.e. all the degrees of freedom which are *not* on the lumen boundary and also not Dirichlet degrees of freedom. It therefore follows that $\mathcal{D}^{\text{lumen}}$ are the degrees of freedom which are on the lumen boundary and subject to Neumann boundary conditions, as discussed in subsubsection 2.1.3.

We define traction as $t_i = P_{ij} n_j$. The second integral in Equation 16 represents the external forces due to the traction applied to the boundary nodes. In the case of the internal nodes, the traction is zero; hence, the second integral in Equation 16 vanishes and the force balance equation reduces to

$$\int_\Omega P_{ij} \frac{\partial N^{a,i}(x)}{\partial x_j} \mathrm{d}\underline{x} = 0 \quad \forall \quad \{a, i\} \in \mathcal{D}^{\text{free}} \; . \tag{17}$$

The imposed Neumann boundary conditions on the lumen boundary provide a force vector f_i^a, such that

$$\int_\Omega P_{ij} \frac{\partial N^a(x)}{\partial x_j} \, \mathrm{d}\underline{x} = f_i^{\text{lumen},a} \quad \forall \quad \{a, i\} \in \mathcal{D}^{\text{lumen}} \; . \tag{18}$$

2.2.5 Linear System of Equations

Equation 17 and Equation 18 form the two force balance equations in the body and at the boundary, respectively. We construct the linear system of equations $A_{ij} \theta_j = b_i$. The matrix A_{ij} represents the coefficients of the linear system, which are obtained by linearising the stress tensor with respect to the shape function and material parameters. The vector θ_j contains the material parameters C_{10} and D_1, which are treated as unknowns in the linear system. The vector b_i represents the vector of external force magnitudes, which is known due to the intraluminal blood pressure. Therefore, the linear system $A_{ij}\theta_j = b_i$ can be solved to obtain the values of the material parameters θ_j that satisfy Equation 17 and Equation 18. Each row in A_{ij} and b_i corresponds to a specific DOF in the system.

The two linear system of equations are defined as

$$A_{ij}^{\text{free}} \cdot \begin{bmatrix} C_{10} \\ D_2 \end{bmatrix} = \underline{0} \qquad \text{and} \qquad A_{ij}^{\text{lumen}} \cdot \begin{bmatrix} C_{10} \\ D_2 \end{bmatrix} = f_i^{\text{lumen},a} \ , \tag{19}$$

where $\underline{0}$ represents a vector of zeros. We concatenate these into one global linear system of equations as

$$\begin{bmatrix} A_{ij}^{\text{free}} \\ \lambda_r A_{ij}^{\text{lumen}} \end{bmatrix} \cdot \begin{bmatrix} C_{10}^{\text{calcified}} \\ D_2^{\text{calcified}} \\ C_{10}^{\text{lipid}} \\ D_2^{\text{lipid}} \\ C_{10}^{\text{intima}} \\ D_2^{\text{intima}} \\ C_{10}^{\text{wall}} \\ D_2^{\text{wall}} \end{bmatrix} = \begin{bmatrix} \underline{0} \\ \lambda_r f_i^{\text{lumen},a} \end{bmatrix} \ . \tag{20}$$

The hyperparameter λ_r is a scalar and affects how much emphasis is given to the lumen force balance equation, with respect to the global linear system of equations (3). It is important to balance the contribution of different terms in the model so that both parts of the force balance contribute correctly in the loss function. We discuss how the tuning of λ_r affects the accuracy of results in subsection 3.1.

2.2.6 Known Parameters

We rearrange $A_{ij}\theta_j = b_i$ for the case of solving for one parameter per domain, where we assume a known value for D_1. This requires removal of the corresponding columns from A_{ij}, such that it reduces from $n_d \times 8$ to $n_d \times 4$. Therefore, the dimensionality of θ_j is also reduced to 4. We consider the known columns from A_{ij} as $A_{i,\text{known}}$ and the rows from θ_j as θ_{known}, such that our linear system of equations becomes

$$A_{ij}\theta_j = b_i - A_{i,\text{known}}\theta_{\text{known}} \ . \tag{21}$$

3 Results

The results of this study are as follows: first, we explore the optimisation method used to solve the linear system of equations and the C_{10} parameters obtained are presented, as well as modifications to the set up to examine the effect of heterogeneity. Second, using the obtained C_{10} parameters, we present stress distributions in the 2D body at different noise levels ($\sigma = 10^{-6}$ and $\sigma = 10^{-3}$ mm). Finally, we present the effect of removing data from the linear system of equations to emulate missing data from clinical images.

3.1 L-BFGS Optimisation & Obtaining C_{10} Parameters

The Limited-memory Broyden–Fletcher–Goldfarb–Shanno (L-BFGS) algorithm provides a numerical optimisation method to deterministically obtain predictions for C_{10} parameters, by iteratively searching for the global minimum of an objective function, in the presence of noise in the displacement measurements. The L-BFGS method allows faster convergence due to approximation of the Hessian matrix (a square matrix which contains information about the curvature of the objective function in each direction) using successive gradients, and uses it to update the search direction and step size, α, in each iteration (26), where α is the size of the step taken towards the minimum of the objective function. Choosing an appropriate value of α is critical for the convergence and stability: if it is too large then the optimiser may overshoot the minimum and diverge; but if it is too small then the convergence will be slow and the optimiser may get stuck in a local minimum. The L-BFGS optimiser does however reduce the step size as the minimum is approached, but a starting value is required. The number of epochs is the number of steps taken during the optimisation process and 10,000 was found to be a sufficient number for convergence, since convergence was seen significantly before this was reached.

The objective, or loss, function is defined as

$$\theta_j^{\text{opt}} = \underset{\theta}{\operatorname{argmin}} \left(||b_i^{\text{free}} - A_{ij}^{\text{free}} \theta_j||^2 + \lambda_r ||b_i^{\text{lumen}} - A_{ij}^{\text{lumen}} \theta_j||^2 \right) \ . \tag{22}$$

It is quadratic in θ_j hence the minimum of the function is when the derivative with respect to θ_j is zero. The first term in the loss function corresponds to the discrepancy between the predicted internal forces and the true external forces on the free region (non-lumen); whereas the second term corresponds to the discrepancy between the predicted internal forces and true external forces acting on the lumen region. The use of λ_r therefore controls the relative importance of these two terms in the optimisation process. If λ_r is large, the optimisation algorithm will prioritise minimising the second term related to the lumen region, but potentially at the expense of higher discrepancies in the free region. On the other hand, if λ_r is small, the algorithm will prioritise minimising the first term, related to the free region, but at the expense of higher discrepancies in the non-lumen region. This is useful in this case since the lumen region, encompassed by the intima, is considerably more important for accurate parameter estimation due to the criteria for a vulnerable plaque.

The metric used to quantify the average difference between the true and predicted parameters is the Root Mean Square Error (RMSE):

$$\text{RMSE} = \sqrt{\frac{1}{n}\sum_i (\theta_i^{\text{true}} - \theta_i^{\text{predicted}})^2}\ , \tag{23}$$

where $n = 4$ is the number of parameters in the vector of C_{10} parameters θ_j. A low RMSE indicates good estimates of the C_{10} parameters, whereas a high RMSE shows that the C_{10} estimates are, on average, significantly different from the true values. We choose to estimate the C_{10} parameters only, using the method described in subsubsection 2.2.6, since attempts to estimate eight parameters (C_{10} and D_1 in each domain) yielded significantly higher RMSE values and less accurate predictions overall.

Two hyperparameters α and λ_r are used, where a hyperparameter refers to a value which is defined before the optimisation begins. We tune them to investigate the relationship between the step size and regularisation parameter on the predictions of C_{10} parameters at increasing noise levels. The L-BFGS optimisation also requires an initial guess of the parameter vector θ_j in order to make initial updates to the direction and step size. Different initialisations were implemented, such as using the exact ground truth values or using zero. However, since the C_{10} parameters can take a wide range of values depending on the plaque's age for example, the chosen vector of initial parameters was [0.1, 0.1, 0.1, 0.1]. This avoids over-reliance on known values as the aim of this work is to test the applicability of EUCLID in clinical scenarios where we do not have access to ground truth values. Finally, a positive constraint was applied so the model can only predict $C_{10} \geq 0$, as the shear modulus cannot be negative. This constraint was applied using a rectified linear unit (ReLU) function.

Figure 4 shows how the RMSE in θ_j changes with respect to increasing noise on the displacement, with multiple combinations of hyperparameters λ_r and α. At no noise ($\sigma = 0$ mm), the estimates of the C_{10} parameters should be close or equal to the ground truth values, such that the RMSE is ≈ 0 kPa, since at this noise level the linear system of equations being solved is the inverse of the boundary problem used to generate the displacement data. It could be argued that this criteria need not be met if the RMSE was low, but $\neq 0$ kPa, and the hyperparameter set showed good generalisation to C_{10} estimations at higher noise levels, as would be indicted by an approximately constant RMSE with increasing noise. However, within the scope of this work, this was not seen, so the process for selected the best set of hyperparameters was the lowest RMSE at the highest noise level.

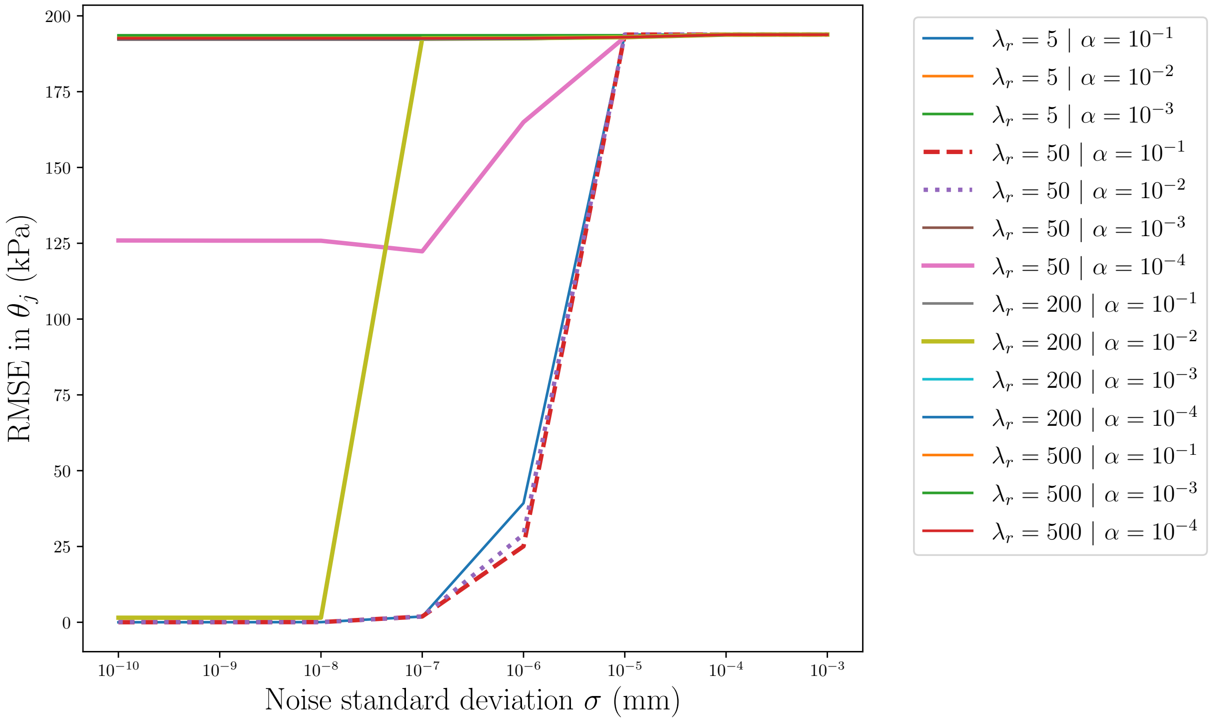

Figure 4: *Root mean square error (RMSE) in the* C_{10} *estimates vector* θ_j *with increasing noise standard deviation (*σ*) on the displacements, with* D_1 *treated as a known value. The legend displays the different combinations of hyperparameters,* λ_r *(regularisation parameter) and* α *(step size), which were used in the L-BFGS optimisation.*

It is clear from Figure 4 that there are multiple hyperparameter sets which do not fulfil this criteria, as shown by a large RMSE ($\approx$ 190 kPa). There are various reasons for why such combinations of λ_r and α cause this, such as λ_r weighting the lumen DOFs too heavily, as seen by a correct estimate of the C_{10} intima value, but at the expense of the other region's C_{10} values. This is typically the case when λ_r is 200 and 500. Additionally, the step size is either too small or large and converges in the wrong global minimum or overshoots it. The hyperparameter set $\lambda_r = 50$ and $\alpha = 10^{-4}$ (pink line on Figure 4) shows a better performance due to a lower RMSE (125 kPa), but does not meet the requirement of accurate predictions at $\sigma = 0$ mm. The hyperparameter set $\lambda_r = 200$ and $\alpha = 10^{-2}$ (green line on Figure 4) shows good parameter estimates until noise level $\sigma = 10^{-8}$ mm, but then shows significant increase in the RMSE at noise level $\sigma = 10^{-7}$ mm.

The three hyperparameter sets denoted by the blue and dashed purple and red lines on Figure 4 show the best combinations, with the set $\lambda_r = 50$ and $\alpha = 10^{-1}$ (red dashed line) as the better of the three due to the slightly lower RMSE value at noise level $\sigma = 10^{-6}$ mm. Table 2 displays the parameters for this set, where we see that the C_{10} values in the calcified and wall regions do not have physically-interpretable estimates at noise level $\sigma = 10^{-5}$ mm, as shown by $C_{10} = 0$ kPa and $C_{10} = 0.13$ kPa, respectively, where the zero value is due to the restriction implemented to ensure there are no negative C_{10} values. The lipid C_{10} value at this noise level (0.081 kPa) represents a 97% deviation from the ground truth value (3.02 kPa). The C_{10} intima value here is 21.08 kPa (37% deviation from the true value of 33.56 kPa), and is the best parameter estimate at this noise level.

σ (mm)	**Calcified**	**Lipid**	**Intima**	**Wall**
ground truth	385.9	3.020	33.56	15.10
0	385.9	3.005	33.56	15.09
10^{-10}	385.9	3.000	33.56	15.09
10^{-9}	385.9	3.000	33.56	15.09
10^{-8}	386.1	3.018	33.56	15.10
10^{-7}	328.1	3.036	33.61	15.14
10^{-6}	327.5	2.826	33.57	14.50
10^{-5}	0	0.081	21.08	0.13
10^{-4}	0	0	0.06	0
10^{-3}	0	0	0	0

Table 2: *C_{10} parameters obtained in each tissue domain at increasing noise standard deviation (σ) from the hyperparameter set $\lambda_r = 50$ and $\alpha = 10^{-1}$ (red dashed line on Figure 4). The ground truth values are displayed in addition to the C_{10} values obtained.*

At $\sigma = 10^{-7}$ mm, we see good accuracy in the C_{10} values of the intima and wall region, with a percentage difference from the ground truth as 0.03% and 3.9%, respectively. The lipid region has a higher deviation with a 9.7% difference. The calcified region has the strongest deviation at this noise level with a value of 14.9%.

Noise level $\sigma = 10^{-6}$ mm is the highest noise level where we still obtain non-zero C_{10} parameters in all four regions. The intima's C_{10} percentage difference increases to 1.43% here. The wall region has a percentage difference of 12.4% and the lipid region's difference is 6.4%. The calcified region increases to 15.0%, which is not a significant increase from $\sigma = 10^{-7}$ mm.

3.1.1 Removing Heterogeneity

We explore the effect that heterogeneity plays on the accuracy of the C_{10} values by removing the degrees of freedom belonging to the calcified region from the linear system of equations $A_{ij}\theta_j = b_i$. This requires removal of one column in A_{ij} and the corresponding row in θ_j, i.e. if the first column is removed in A_{ij} then the first row in θ_j must also be removed. Additionally, the rows corresponding to calcified DOFs in A_{ij} and b_i must also be removed from the calculations. The displacement data is generated considering the full heterogeneity of the body, i.e., the full-body strain information is accurately produced, ensuring a physically admissible force balance, but the calcified DOFs are removed afterwards. Within the context of this study, this approach is justifiable given the importance of accurately predicting the parameter for the intima region encompassing the fibrous cap. Although one could argue that DOFs corresponding to the lipid and wall regions could also be removed to further reduce complexity, the primary objective of this work is to investigate the limits of parameter determination with EUCLID in the presence of heterogeneity. Consequently, systematically eliminating complexity until homogeneity is achieved would not align with the aims of this thesis investigation.

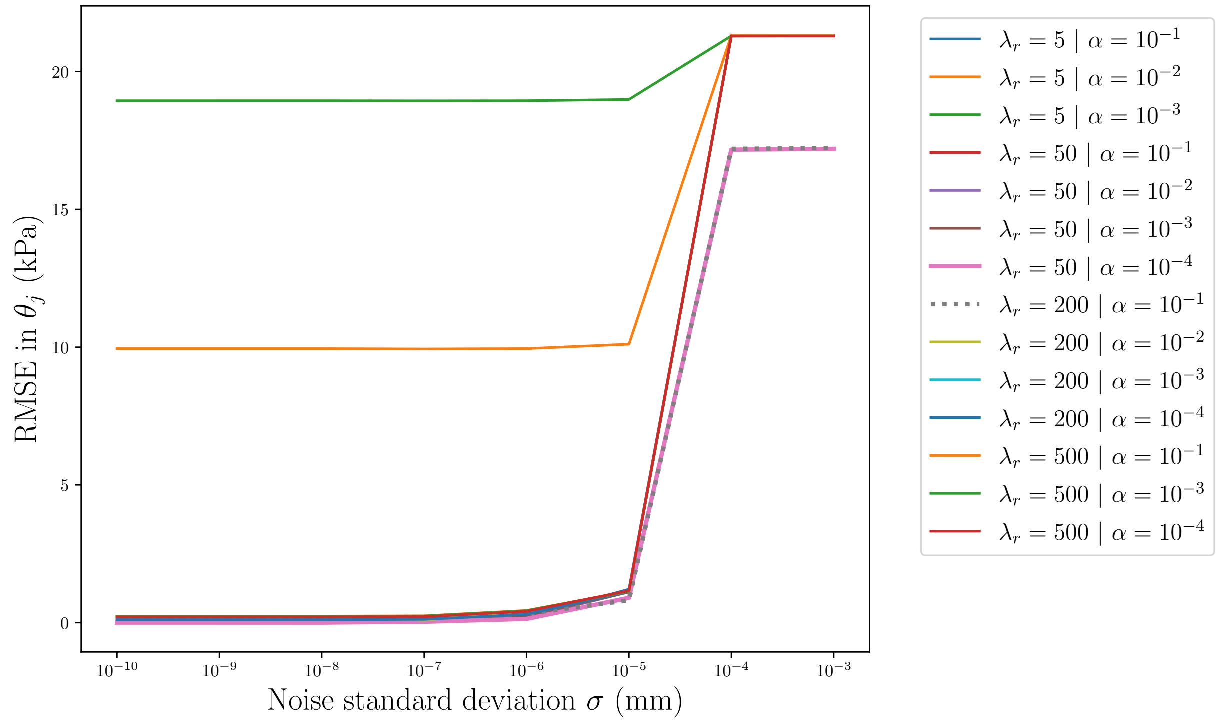

Figure 5: **No calcified DOFs.** *Root mean square error (RMSE) in the C_{10} estimates vector θ_j with increasing noise standard deviation on the displacements, with D_1 treated as a known value. The legend displays the different combinations of hyperparameters, λ_r (regularisation parameter) and α (step size), which were used in the L-BFGS optimisation.*

The magnitude of the RMSE is lower in Figure 5 with the calcified DOFs removed, as shown by a maximum at $\approx$ 21 kPa. This is expected since deviations from the true calcified C_{10} value are larger in magnitude due to the relatively larger C_{10} value (385.9 kPa). However, the performance of determining the three C_{10} parameters is in general better without the calcified DOFs, as can be seen in Table 3, where the obtained parameters are displayed from the hyperparameter set $\lambda_r = 50$ and $\alpha = 10^{-4}$. There is no significantly better performing combination of λ_r and α in this set up (as shown by the multiple lines trending in the same way on Figure 5), so the values displayed in Table 3 serve to highlight the improvement in parameters without calcified DOFs. These values are an improvement from those displayed in Table 2 since the error on the intima C_{10} at noise level $\sigma = 10^{-5}$ mm is 10.4%, compared to 37% seen in Table 2. The C_{10} parameter obtained for the lipid region at this noise level yielded a percentage error of 13.2%, an improvement of 84% from the results with all regions. The C_{10} parameter in the wall region shows an 86% improvement, with a deviation from the ground truth as 12.1%.

σ (mm)	**Lipid**	**Intima**	**Wall**
ground truth	3.020	33.56	15.10
0	3.019	33.56	14.96
10^{-10}	3.019	33.56	14.96
10^{-9}	3.019	33.56	14.96
10^{-8}	3.018	33.55	14.96
10^{-7}	3.034	33.61	14.96
10^{-6}	3.151	33.57	14.98
10^{-5}	2.627	30.07	13.27
10^{-4}	0.098	8.28	0.099
10^{-3}	0.090	0	0.098

Table 3: **No calcified DOFs.** *C_{10} parameters obtained in three tissue domains (lipid, wall and intima) at increasing noise standard deviation (σ) from the hyperparameter set $\lambda_r = 50$ and $\alpha = 10^{-4}$ (pink line on Figure 4). The ground truth values are displayed in addition to the C_{10} values obtained.*

In this set up, the smaller λ_r value of 5 is not favourable, since the two lines (green and orange) which do not meet the requirement of RMSE = 0 kPa at low noise belong to this value. We can then conclude that the effect of the combination of hyperparameters with λ_r =50, 200 or 500 is minimal, showing that the L-BFGS can sufficiently optimise the loss function until $\sigma = 10^{-5}$ mm. A possible reason for this is that there is one pronounced global minimum in the loss function when the calcified region is removed, making convergence to a solution of θ_j less complex.

3.2 Stress Distributions

The RMSE is calculated for the whole C_{10} solution vector θ_j and therefore provides an overview of the optimiser's predictions as a whole; however, the RMSE can be dominated by poor predictions in particular regions. In particular, the calcified region is where we see the accuracy in the obtained C_{10} value deteriorate first. While the RMSE provides insight into the overall performance, the aim of the this research is to be able to predict parameters under clinical imaging conditions in order to classify a vulnerable atherosclerotic plaque. Therefore, we consider the stress distributions based on the noisy displacement data and the predicted parameters in each domain, with a known D_1 value, as shown by the middle columns in Figure 7 and Figure 8. The 12 subfigures presented in each of these figures represent each component of the first Piola-Kirchhoff stress tensor P_{ij} in 2D (P_{xx}, P_{xy}, P_{yx} and P_{yy}). True stress distributions are shown as a comparison in the first column, calculated from ground truth C_{10} values and true displacement data. The difference between the predicted and the true values ΔP_{ij} is displayed in the third column.

The stress distributions at noise levels $\sigma = 10^{-6}$ and 10^{-3} mm are displayed: the former is the highest noise level where the C_{10} values in all domains are physically relevant; and the latter is shown as this is the expected level of noise in clinical imaging, as discussed in subsubsection 2.1.5. Table 6 and Table 5 provide the mean P_{ij} values as a guide for second column of the stress distributions. Due to the multiple orders of magnitude across the regions, we display the stress using a logarithmic scale. This requires the absolute value of the stress components to be used, so we lose clarity about whether elements are in compression or tension, but within the scope of this research the figures provided are deemed sufficient since we are interested in the stress magnitude. Each subfigure has its own scale depending on the range of data present in that distribution and the figures are made with the hyperparameter set $\lambda_r = 50$ and $\alpha = 1 \times 10^{-1}$.

The calcified region is the small region in Figure 7 (see Figure 6 for domains). It is this region where significant deviation from the C_{10} parameter and the resulting stress distribution is seen at the lowest noise level. This deviation is shown by a percentage difference from the true mean stress $\bar{P}_{ij}$ of 99% in all four regions. This large percentage difference is however not observed in the intima, wall and lipid regions. In the lipid and intima regions, we see good agreement with the true $\bar{P}_{ij}$ values, as shown by percentage differences of $\approx 6\%$ in the lipid region, and $\approx 2\%$ in the intima region. The percentage difference from the wall region's true $\bar{P}_{ij}$ is slightly larger at $\approx 12\%$.

Figure 8 shows the stress distributions at $\sigma = 10^{-3}$ mm, produced using the obtained

C_{10} values (Table 2) and the true D_1 values. The obtained values for C_{10} are all 0 kPa, hence the stress components in all regions show a close-to-zero distribution (highlighted in Table 6). Physically, this implies that the body is in a state of mechanical equilibrium, where the external forces acting (blood pressure force) are balanced by the internal forces within the body. However, since in this case the body is subject to deformation by an intraluminal pressure of 120 mmHg (15.96 kPa), there should be resultant internal stresses, as we see deformation (as shown by the strain map in **??** in subsection A.2). A deformation is a result of a stress which itself is caused by a force, and the strain map, which shows the distribution of strains throughout the 2D body, is a direct consequence of the internal stresses caused by the external force.

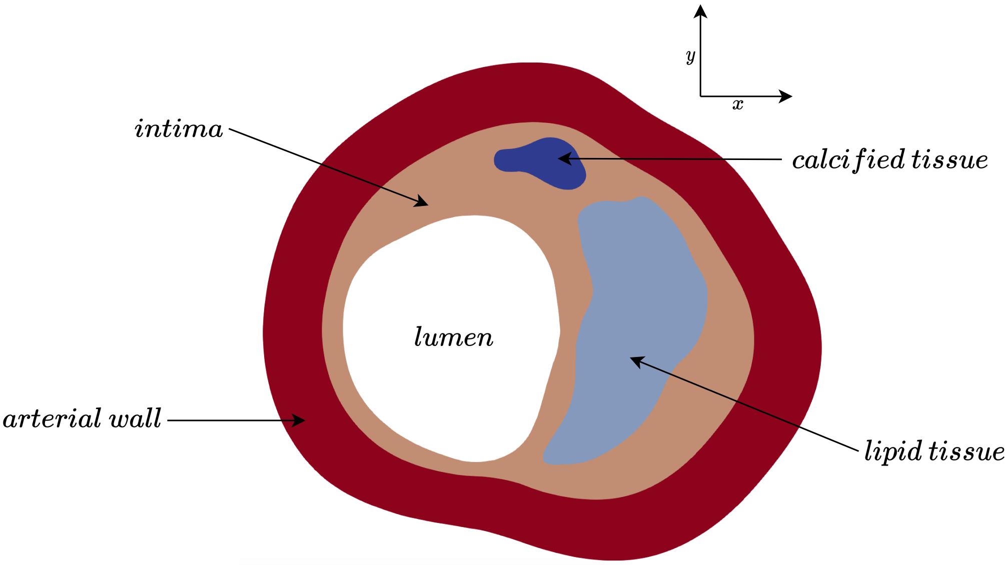

Figure 6: *The regions of the 2D heterogeneous body are displayed for comparison to the stress distributions shown in Figure 7 and Figure 8. The x and y directions are also shown.*

Tissue	$\boldsymbol{\bar{P}_{xx}}$	$\boldsymbol{\bar{P}_{xy}}$	$\boldsymbol{\bar{P}_{yx}}$	$\boldsymbol{\bar{P}_{yy}}$
Calcified	8.52 ± 7.00	5.51 ± 3.04	5.51 ± 3.04	8.65 ± 7.16
Lipid	1.36 ± 0.99	1.27 ± 0.63	1.28 ± 0.64	1.04 ± 0.70
Intima	7.86 ± 6.85	7.26 ± 6.18	7.41 ± 7.02	7.80 ± 6.79
Wall	2.24 ± 2.26	2.11 ± 1.92	2.12 ± 1.94	2.23 ± 2.25

Table 4: **No noise**. *True mean ($\bar{P}_{ij}$) ± standard deviation (kPa) of the stress distribution values without noise in each tissue region.*

Tissue	$\boldsymbol{\bar{P}_{xx}}$	$\boldsymbol{\bar{P}_{xy}}$	$\boldsymbol{\bar{P}_{yx}}$	$\boldsymbol{\bar{P}_{yy}}$
Calcified	0.072 ± 0.059	0.047 ± 0.026	0.046 ± 0.026	0.074 ± 0.060
Lipid	1.27 ± 0.93	1.19 ± 0.58	1.20 ± 0.60	0.97 ± 0.65
Intima	7.75 ± 6.76	7.16 ± 6.71	7.31 ± 6.93	7.96 ± 6.69
Wall	1.97 ± 1.98	1.85 ± 1.69	1.86 ± 1.70	1.96 ± 1.97

Table 5: **Noise level $\boldsymbol{\sigma = 10^{-6}}$ mm**. *Mean ($\bar{P}_{ij}$) ± standard deviation (kPa) of the predicted stress distributions, in each of the four domains, produced with noisy displacement data and the obtained C_{10} values. D_1 values are assumed to be known. These values supplement the second column of figures in Figure 7.*

Tissue	$\boldsymbol{\bar{P}_{xx}}$	$\boldsymbol{\bar{P}_{xy}}$	$\boldsymbol{\bar{P}_{yx}}$	$\boldsymbol{\bar{P}_{yy}}$
Calcified	$(3.56 \pm 2.69) \times 10^{-6}$	$(9.91 \pm 12.9) \times 10^{-8}$	$(9.14 \pm 10.6) \times 10^{-8}$	$(3.59 \pm 2.70) \times 10^{-6}$
Lipid	$(4.79 \pm 3.63) \times 10^{-4}$	$(3.63 \pm 4.01) \times 10^{-5}$	$(6.63 \pm 7.13) \times 10^{-5}$	$(4.08 \pm 3.11) \times 10^{-4}$
Intima	$(4.23 \pm 3.27) \times 10^{-5}$	$(3.10 \pm 4.20) \times 10^{-6}$	$(4.79 \pm 7.09) \times 10^{-6}$	$(4.31 \pm 3.31) \times 10^{-5}$
Wall	$(8.28 \pm 6.40) \times 10^{-5}$	$(3.38 \pm 4.04) \times 10^{-6}$	$(5.06 \pm 6.38) \times 10^{-6}$	$(8.31 \pm 6.39) \times 10^{-5}$

Table 6: **Noise level $\boldsymbol{\sigma = 10^{-3}}$ mm**. *Mean ($\bar{P}_{ij}$) ± standard deviation (kPa) of the predicted stress distributions, in each of the four domains, produced with noisy displacement data and the obtained C_{10} values. D_1 values are assumed to be known. These values supplement the second column of figures in Figure 8.*

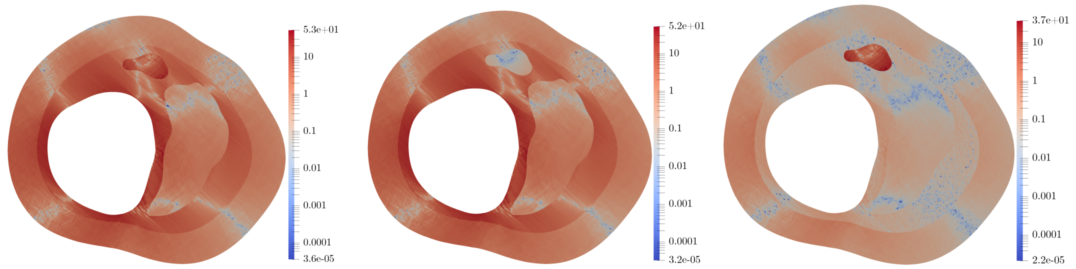

True P_{xx} Predicted P_{xx} ΔP_{xx}

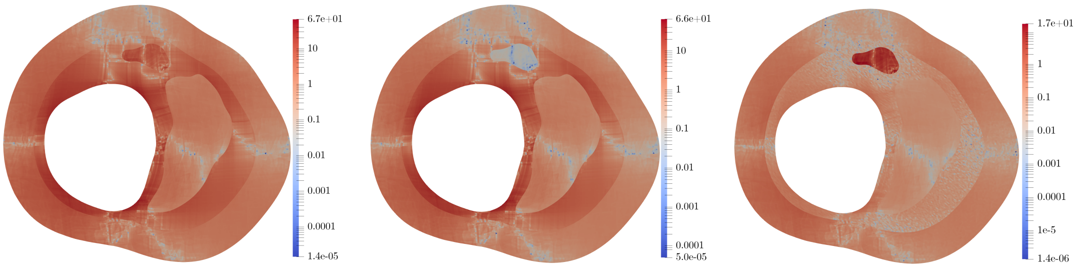

True P_{xy} Predicted P_{xy} ΔP_{xy}

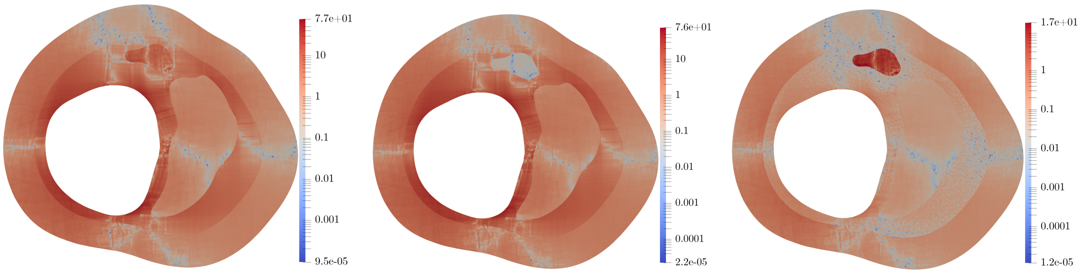

True P_{yx} Predicted P_{yx} ΔP_{yx}

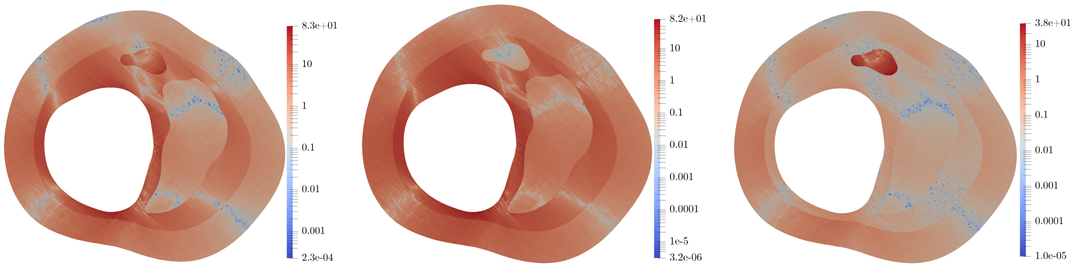

True P_{yy} Predicted P_{yy} ΔP_{yy}

Figure 7: **Noise level $\sigma = 10^{-6}$ mm.** *Components of the first Piola-Kirchhoff stress tensor P_{ij}. Deformed by 120 mmHg (15.96 kPa). The first column represents the true stress distributions. The second column represents the predicted stress distribution with noisy displacement data and the obtained C_{10} values from the L-BFGS loss function optimisation. The third column shows the absolute error between the true and predicted distributions.*

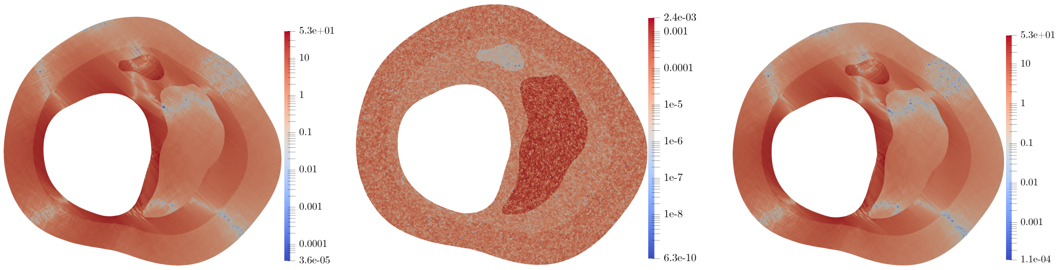

True P_{xx} Predicted P_{xx} ΔP_{xx}

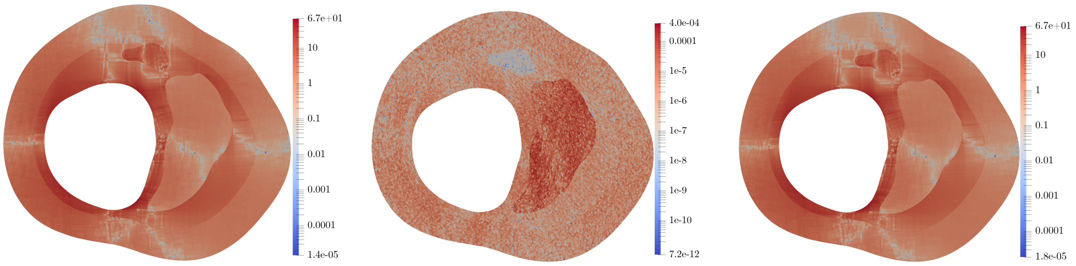

True P_{xy} Predicted P_{xy} ΔP_{xy}

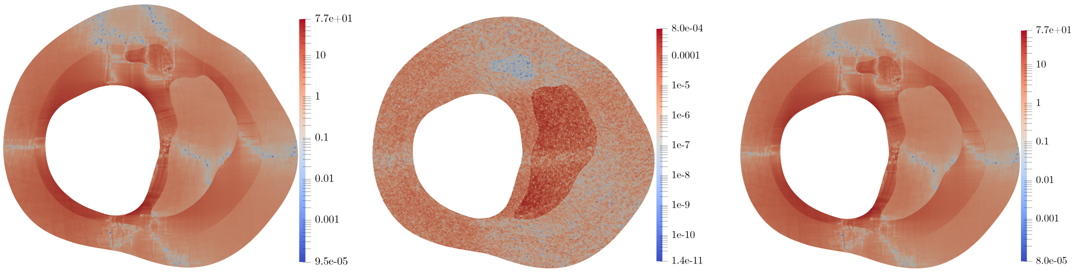

True P_{yx} Predicted P_{yx} ΔP_{yx}

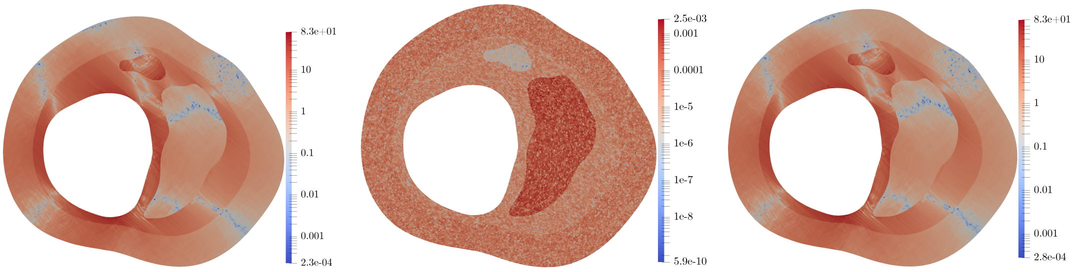

True P_{yy} Predicted P_{yy} ΔP_{yy}

Figure 8: **Noise level $\boldsymbol{\sigma = 10^{-3}}$ mm.** *Components of the first Piola-Kirchhoff stress tensor P_{ij}. Deformed by 120 mmHg (15.96 kPa). The first column represents the true stress distributions. The second column represents the predicted stress distribution with noisy displacement data and the obtained C_{10} values from the L-BFGS loss function optimisation. The third column shows the absolute error between the true and predicted distributions.*

3.3 Systematic Data Reduction

We systematically reduce the data in the linear system of equations, i.e. the number of rows in A_{ij} and b_i are reduced. Heat maps are shown for different percentages of the total number of rows (32,704), up until 0.06%, where each row represents a DOF in the 2D heterogeneous body. This is analogous to receiving a DIC image with missing data, which is commonplace due to noise in measurements or the software lacking displacement information in certain regions, hence the model would be working with an incomplete displacement field. The aim of this is to understand how the optimiser performs under these conditions, and to determine the minimum data requirement for achieving accurate results. As the results presented in previous sections do not meet the expected noise level present in clinical images, the purpose of this is to compare the results of L-BFGS with the full set of DOFs (100% of DOFs as displayed on the figures). This tells us the robustness of the optimiser from which we can gain insights into the applicability of using it in real-world situations where the data availability may be less than ideal. As in subsection 3.2, we use the L-BFGS optimiser with the regularisation parameter $\lambda_r = 50$ and the step size $\alpha = 10^{-1}$.

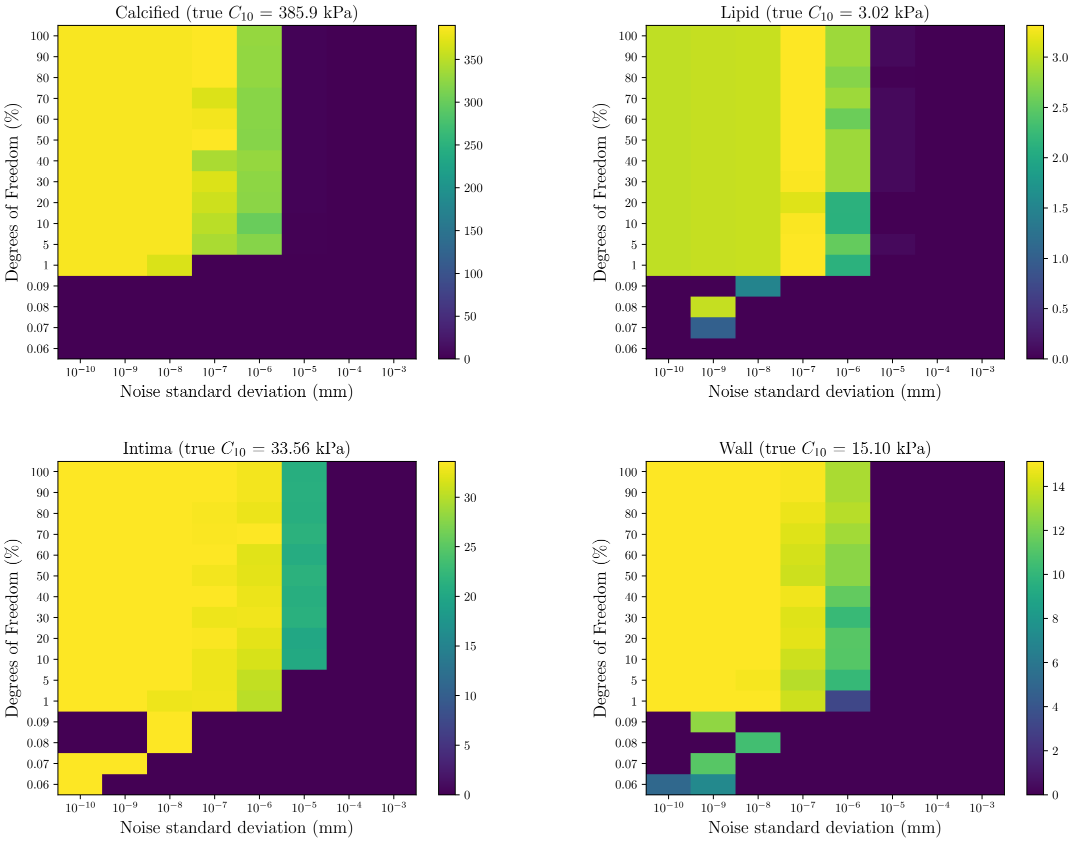

Figure 9: *C_{10} parameters as a function of percentage of DOFs and noise level, in each of the four domains. The C_{10} parameters are estimated using the L-BFGS optimisation with λ_r = 50 and $\alpha = 10^{-1}$.*

The heat maps presented in Figure 12 show that at noise level $\sigma = 10^{-10}$ to 10^{-8} mm, the values obtained for the C_{10} parameters are accurate until 1% of the total DOFs used in the calculations in all four domains, where 1% of the total number gives an integer value of 327 DOFs. Below this number of DOFs, for all four of the domains, the L-BFGS optimiser could not obtain any non-zero C_{10} values.

The largest effect of data reduction is seen in the calcified region, where accuracy of C_{10} parameters at the 1% of DOFs level deteriorates prematurely relative to higher percentages (DOFs $\geq$ 5%). At this percentage, $C_{10} = 0$ kPa at a noise level of $\sigma = 10^{-7}$ mm, with deviation from the ground truth already occurring at $\sigma = 10^{-8}$ mm (two orders of magnitude before the other regions at the same percentage level), although the deviation is not significant at 1.4%. This can be explained by the method used to perform this test: the sampled rows are randomly selected, thus the likelihood of a row which corresponds to any DOF in the calcified domain is far smaller than any other region, as a result of these DOFs comprising only 2% of the total number of DOFs.

The lipid and wall regions show similar behaviour as the displacement data is reduced, in that they both make give non-zero C_{10} values at $\sigma = 10^{-6}$ mm. At noise levels above this the C_{10} values obtained are 0 kPa. At $\sigma = 10^{-6}$ mm in the lipid region, there is no correlation between the percentage of DOFs used, as shown by random fluctuations in the parameters obtained. The wall region, on the other hand, sees some correlation with the percentage of DOFs; fewer DOFs means the accuracy in the parameter suffers. A possible reason for why the obtained C_{10} values in these regions behave in a similar way is due to their proximity to the lumen, meaning they are more affected by the applied pressure force, as well as lower ground truth stiffnesses, hence more deformation and consequently higher signal-to-noise ratio relative to the calcified region. There are more DOFs in the wall than the lipid region (40% compared to 17% of the total), which is a possible explanation for the slightly better C_{10} estimates at noise level $\sigma = 10^{-5}$ mm for DOFs $\geq$ 5%.

The intima region shows the same trend as the other three regions as the C_{10} values yielded at noise $\sigma = 10^{-10}$ mm and below 1% DOFs are physically unrealistic ($C_{10} = 0$ kPa). Accuracy relative to the true C_{10} value is maintained until 1 % DOFs at noise $\sigma = 10^{-5}$ mm. At noise level $\sigma = 10^{-4}$ mm, the C_{10} value is obtained as $\approx$ 21 kPa, as seen is subsection 3.1, but this is only maintained until 10% DOFs. Furthermore, it must be noted that in this region and the lipid and wall regions there are some C_{10} values obtained as low as 0.06% and 0.07%, but there is no clear correlation here. The reason for this is unclear since this method uses the same set of randomly selected rows for a given percentage level, so if C_{10} values are obtained at $\sigma = 10^{-8}$ mm, for example, then values should also be obtained at $\sigma = 10^{-10}$ mm.

The linear system of equations is robust until 10% total DOFs in the intima region and 1% in the calcified, lipid and wall regions, where robustness is evaluated against the values obtained with 100% DOFs. Since the intima region contains the fibrous cap, it is more important for parameter and stress distribution prediction, hence we conclude that 10% of the displacement data is required for obtaining C_{10} values in this way.

4 Discussion

The aim of this study was to test the applicability and performance of EUCLID for the material characterisation of multicomponent atherosclerotic plaques. Specifically, we sought to obtain the C_{10} neo-Hookean material parameters in a 2D finite element body. The geometry was based on a cross-section of an atherosclerotic diseased artery with four domains, where the domains themselves were considered to be homogeneous. A plane strain assumption was used, along with a near-incompressibility assumption of $\nu = 0.49$. Gaussian noise was artificially added in order to emulate IVUS images. The aim was to be able to predict material parameters at an expected displacement noise standard deviation $\sigma = 1$ μm (10^{-3} mm). Displacement data was generated using the FEM with all material points modelled as a neo-Hookean solid to capture any potential non-linear behaviour. Mechanical loading was done via intraluminal blood pressure of 120 mmHg to mimic arterial expansion. The objective function (Equation 22) was minimised using the L-BFGS optimisation algorithm. This function represents the residual error between the predicted internal forces ($A_{ij}\theta_j$) and the true external forces (b_i), and was defined as the L_2 norm. θ_j is the solution vector containing the domain-dependent C_{10} neo-Hookean parameters.

Results were presented in the form of the RMSE as a function of displacement noise standard deviation σ, obtained C_{10} values, stress distributions and systematic data reduction. The RMSE shows the accuracy in the whole solution vector θ_j, whilst the stress distributions calculated from the C_{10} values and noisy displacement data highlighted specific regions in the heterogeneous body where accuracy suffered. The RMSE was displayed to convey the impact of different sets of hyperparameters λ_r and α. When using all regions, i.e. when the solution vector θ_j contains four C_{10} values, $\lambda_r = 50$ was found to be optimal. This regularisation parameter weights the relative contribution of lumen (boundary) and non-lumen (internal) in the objective function. A value of 50 also corresponds to the ratio of non-lumen to lumen DOFs. The stress distributions highlight the effect of the deviation of the calcified C_{10} parameter at $\sigma = 10^{-6}$ mm, where a 15% deviation from the true C_{10} value caused a loss in accuracy of 99% compared to the true mean stress distribution, in each stress component P_{ij}. However, this deviation in the stress calculation is also in part due to the noise added to the displacements.

Removing the calcified DOFs (subsubsection 3.1.1) improved the accuracy of the model, suggesting that the heterogeneity of the 2D finite element body impacts the model's accuracy. The improvement in C_{10} parameter accuracy without calcified DOFs was also seen in the intima, lipid and wall regions. Furthermore, the heat maps (Figure 12) show that using 10% of the total data yields accurate C_{10} parameters in the four regions, where accuracy was compared to the full data-set (100% DOFs).

Overall, the method fails to replicate stress distributions in any significant range at the desired noise level of 10^{-3} mm. The highest noise level where accuracy was maintained in the stress distributions and C_{10} parameters obtained was 10^{-6} mm, suggesting this method requires improvement for the applicability of plaque risk assessment in a clinical setting. The estimated stress distribution within each region at 10^{-3} mm resulted in an effective stress of 0 kPa, indicating an equilibrium distribution. This presents a challenge in assessing the risk of atherosclerotic plaque, as a low predicted stress level may erroneously suggest a low risk of plaque rupture. Therefore, the algorithm's current form, with positive constraints enforced on the C_{10} parameters or fine-tuning the λ_r and α hyperparameters, is insufficient for this boundary value problem. Possible reasons for this are the small displacements and resulting small strains due to the intraluminal pressure (displayed in subsection A.2), as well as the heterogeneity present in the 2D finite element body. The small displacements impact the signal-to-noise ratio (SNR), which is calculated as

$$\text{SNR} = \frac{P_{signal}}{P_{noise}} , \tag{24}$$

where P_{signal} and P_{noise} represent the power of the signal and noise, respectively. The SNR is calculated using the maximum power of the signal, in this case the maximum displacement which is of the order of 10^{-1} mm (as shown in subsection A.1). At the expected IVUS noise level 10^{-3} mm, this yields a SNR of 10^2. However, for the accuracy of C_{10} parameters required at $\sigma = 10^{-7}$ mm (RMSE $\approx$ 0 kPa), the L-BFGS optimiser requires at least a SNR of 10^5. Sufficient predictions are made in three regions (excluding the calcified region) at $\sigma = 10^{-5}$ mm, where a SNR of 10^3 would be required. Although the SNR is calculated with the maximum signal, the displacements in the calcified region, especially in the y direction, are typically 10^{-2} mm which is an order of magnitude smaller than in the intima region, thus resulting in SNR an order of magnitude lower. This is due to the higher shear modulus in the calcified region, as well as it being the furthest away from the applied force at the lumen boundary. This means that any force applied at the boundary will need to be transmitted across more nodes, and the internal stresses caused by this force will yield smaller strains. Additionally, this is the smallest region, accounting for only 2% of the total elements. Therefore, the calcified C_{10} parameter occurs in fewer equations in the system of equations. This effect is especially prevalent in the case where the lumen DOFs are weighted with a higher value of λ_r, since the relative importance of the calcified DOFs decreases. Overall, the small strains encountered in this deformation pose a challenge to this method, as they are more susceptible to errors in the predictions.

The heterogeneity defined in this work also reduces the accuracy of parameters obtained at higher noise levels, as reflected by a reduction in the RMSE (Figure 5), as well as an increase in accuracy of the C_{10} parameters in $\sigma = 10^{-5}$, relative to the case with all regions, showing improvement in the noise performance by one order of magnitude. As discussed previously, this approach is valid to both explore the effect of obtaining parameters in a multicomponent domain, and because the intima region is of more significance during plaque risk assessment. To this end, future work could explore parameter estimation in a heterogeneous intima region.

In this work the ground truth values are known which mean that the errors calculated are with respect to the ground truth. In a clinical setting the ground truth estimates are not known. In such a case, the proposed technique requires further research in order to reach state-of-the-art noise levels in clinical imaging devices. In conclusion, the L-BFGS optimiser's performance in predicting the C_{10} neo-Hookean parameters is limited by the noise level in the input data and the heterogeneity of the 2D finite element body. Future research could investigate alternative optimisation algorithms or techniques to improve the model's accuracy under these conditions. Furthermore, the role of the heterogeneity could be further explored by using different geometries which would allow the effect of the distance of domains from the applied forces, or the sizes of domains to be properly quantified. Additionally, different constraints within the optimisation procedure could be explore, such as using reasonable estimates of the orders of magnitudes of parameters, rather than just defining that $C_{10} > 0$ kPa, since this resulted in highly inaccurate stress distributions at the expected noise level. Techniques to de-noise the displacement data could also be explored.

5 Conclusion

This work has explored the use of EUCLID, a computational framework based on discovering constitutive models without stress data, for determining four domain-dependent neo-Hookean constants C_{10} using noisy displacement data. The aim of this was to test whether it could aid in the risk assessment of atherosclerotic plaques as the stress distributions, particularly in the intima region overlying the lipid core, are a key indicator of plaque vulnerability. Whilst good accuracy was observed in the stress distributions at $\sigma = 10^{-5}$ mm in the intima, wall and lipid regions, the expected level of noise (10^{-3} mm) yielded physically unrealistic stress distributions. This poses as the key limitation of this work; however, the method is robust against missing data. This was highlighted by accuracy in the four C_{10} parameters obtained until 10% of the total DOFs, with 1% being achieved in some regions. This signifies that if improvements are made to the optimisation method and/or displacement data is significantly denoised, this framework could still have implications in the risk assessment of atherosclerotic plaques.

A Appendix

A.1 Displacement Histograms

The absolute displacements in each direction and in each of the four domains are presented, to convey the magnitude of the signal present in the displacement data. The directions x and y are displayed separately, rather than the magnitude of the displacement vector ($\sqrt{u_x^2 + u_y^2}$) as the linear system of equations is defined in terms of degrees of freedom. Each degree of freedom represents either the x or y direction of a node in the finite element body.

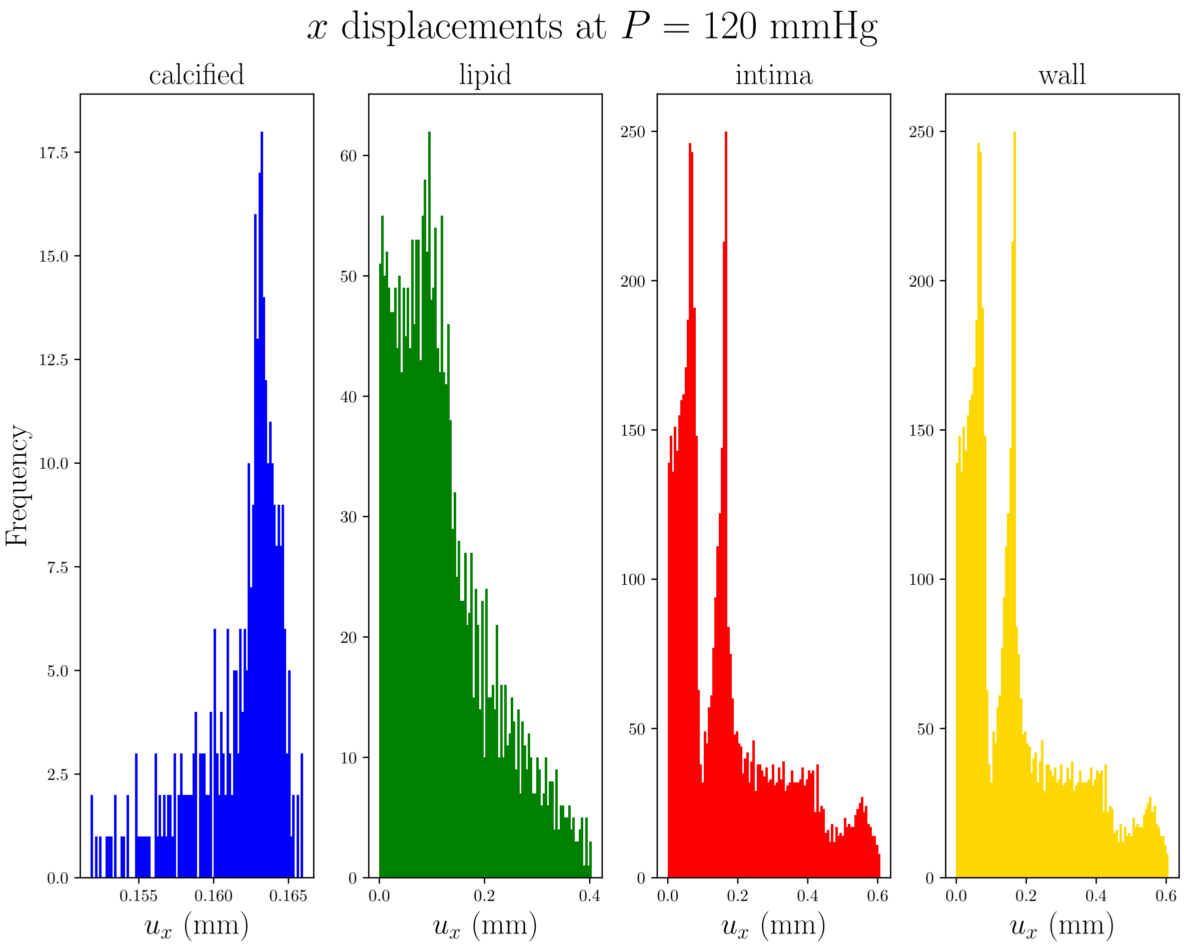

Figure 10: *Displacements in the x direction due to an intraluminal pressure of* 120*mmHg (15.96 kPa). The four domains calcified, lipid, intima, wall are displayed separately in blue, green, red and yellow, respectively.*

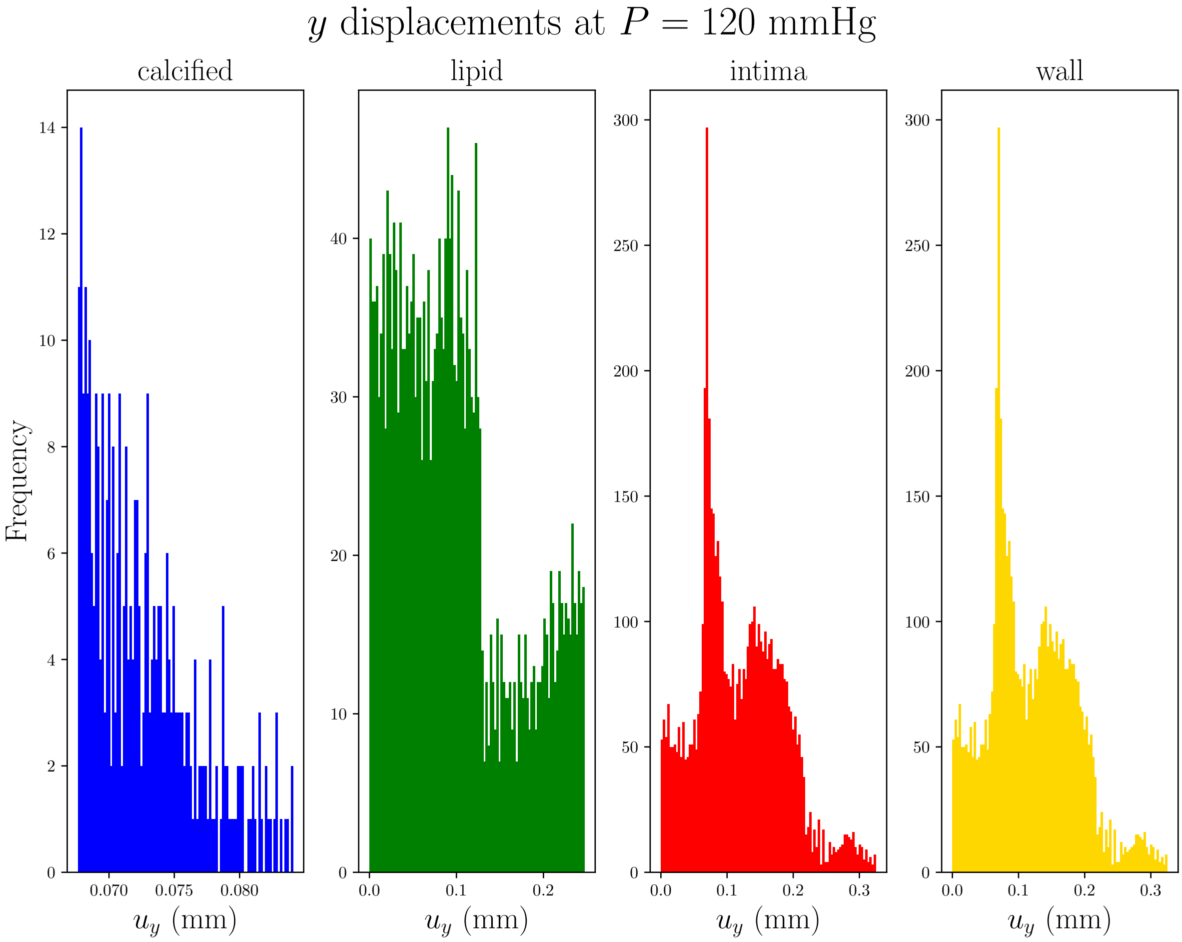

Figure 11: *Displacements in the* y *direction due to an intraluminal pressure of* 120 *mmHg (15.96 kPa). The four domains calcified, lipid, intima, wall are displayed separately in blue, green, red and yellow, respectively.*

A.2 Strain Distribution at 120 mmHg

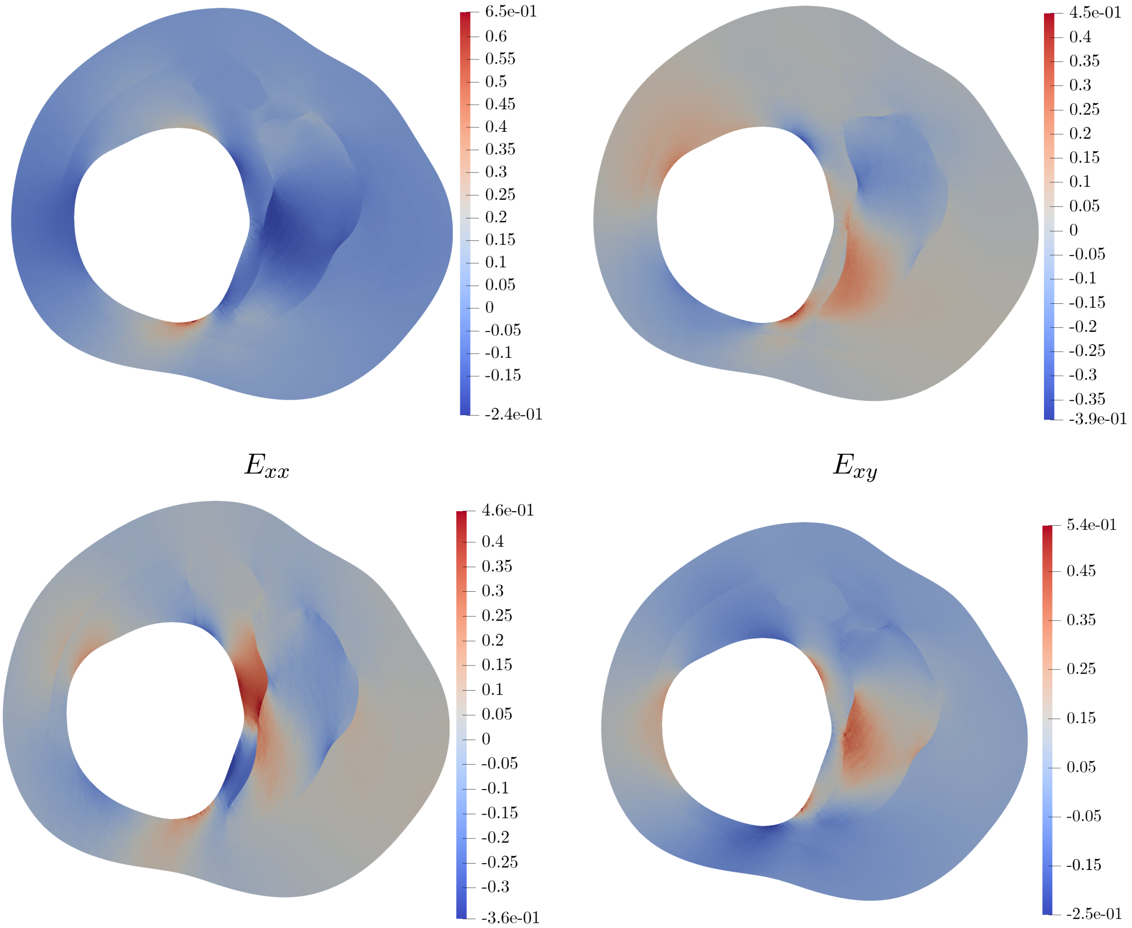

E_{xx} E_{xy}

E_{yx} E_{yy}

Figure 12: *Green-Lagrange Strain Tensor (E) components in 2D at 120 mmHg.*

A.3 First Piola-Kirchhoff Stress Components

We define the determinant of the deformation gradient tensor $\det F_{ij} = F_{11}F_{22} - F_{12}F_{21}$. The four components of the first Piola-Kirchhoff stress tensor P_{ij} in two-dimensions are:

$$P_{11} = \left(\frac{2F_{11}}{\det(F_{ij})^{\frac{2}{3}}} - \frac{2F_{22}(1 + F_{11}^2 + F_{12}^2 + F_{21}^2 + F_{22}^2)}{3\det(F_{ij})^{\frac{5}{3}}} \right) C_{10} + 2F_{22}(\det(F_{ij}) - 1)D_1 \quad (25)$$

$$P_{12} = \left(\frac{2F_{12}}{\det(F_{ij})^{\frac{2}{3}}} + \frac{2F_{21}(1 + F_{11}^2 + F_{12}^2 + F_{21}^2 + F_{22}^2)}{3\det(F_{ij})^{\frac{5}{3}}} \right) C_{10} - 2F_{21}(\det(F_{ij}) - 1)D_1 \quad (26)$$

$$P_{21} = \left(\frac{2F_{21}}{\det(F_{ij})^{\frac{2}{3}}} + \frac{2F_{12}(1 + F_{11}^2 + F_{12}^2 + F_{21}^2 + F_{22}^2)}{3\det(F_{ij})^{\frac{5}{3}}} \right) C_{10} - 2F_{12}(\det(F_{ij}) - 1)D_1 \quad (27)$$

$$P_{22} = \left(\frac{2F_{22}}{\det(F_{ij})^{\frac{2}{3}}} - \frac{2F_{11}(1 + F_{11}^2 + F_{12}^2 + F_{21}^2 + F_{22}^2)}{3\det(F_{ij})^{\frac{5}{3}}} \right) C_{10} + 2F_{11}(\det(F_{ij}) - 1)D_1 \quad (28)$$

References

[1] M. Vaduganathan, G. A. Mensah, J. V. Turco, V. Fuster, and G. A. Roth, "The Global Burden of Cardiovascular Diseases and Risk: A Compass for Future Health," *Journal of the American College of Cardiology*, vol. 80, pp. 2361–2371, 12 2022.

[2] W. Wang, M. Liang, L. Wang, W. Bei, X. Rong, J. Xu, and J. Guo, "Role of prostaglandin E2 in macrophage polarization: Insights into atherosclerosis," *Biochemical Pharmacology*, vol. 207, 1 2023.

[3] M. Flaschel, S. Kumar, and L. De Lorenzis, "Unsupervised discovery of interpretable hyperelastic constitutive laws," *Computer Methods in Applied Mechanics and Engineering*, vol. 381, 8 2021.

[4] M. Flaschel, S. Kumar, and L. De Lorenzis, "Discovering plasticity models without stress data," *npj Computational Materials*, vol. 8, no. 91, 2022.

[5] P. Thakolkaran, A. Joshi, Y. Zheng, M. Flaschel, L. De Lorenzis, and S. Kumar, "NN-EUCLID: deep-learning hyperelasticity without stress data," *Journal of the Mechanics and Physics of Solids*, vol. 169, no. 105076, 2022.

[6] A. Joshi, P. Thakolkaran, Y. Zheng, M. Escande, M. Flaschel, L. De Lorenzis, and S. Kumar, "Bayesian-EUCLID: Discovering hyperelastic material laws with uncertainties," *Computer Methods in Applied Mechanics and Engineering*, vol. 398, p. 115225, 8 2022.

[7] M. E. Boesen, D. Singh, B. K. Menon, and R. Frayne, "A systematic literature review of the effect of carotid atherosclerosis on local vessel stiffness and elasticity," *Atherosclerosis*, vol. 243, pp. 211–222, 11 2015.

[8] G. Qin, L. Wang, Y. Hua, H. Hou, Q. Zou, D. Wang, Z. Hu, and D. Lu, "Comparative morphology of the internal elastic lamina of cerebral and peripheral arteries," *International Journal of Clinical and Experimental Pathology*, vol. 13, no. 4, p. 764, 2020.

[9] A. C. Doran, N. Meller, and C. A. McNamara, "Role of Smooth Muscle Cells in the Initiation and Early Progression of Atherosclerosis," *Arteriosclerosis, Thrombosis, and Vascular Biology*, vol. 28, pp. 812–819, 5 2008.

[10] D. Hu, C. Yin, S. Luo, A. J. Habenicht, and S. K. Mohanta, "Vascular Smooth Muscle Cells Contribute to Atherosclerosis Immunity," *Frontiers in Immunology*, vol. 10, no. MAY, p. 1101, 2019.

[11] S. Z. Gu and M. R. Bennett, “Plaque Structural Stress: Detection, Determinants and Role in Atherosclerotic Plaque Rupture and Progression,” *Frontiers in Cardiovascular Medicine*, vol. 9, p. 875413, 7 2022.

[12] H. E. Barrett, K. Van der Heiden, E. Farrell, F. J. Gijsen, and A. C. Akyildiz, “Calcifications in atherosclerotic plaques and impact on plaque biomechanics,” *Journal of Biomechanics*, vol. 87, pp. 1–12, 4 2019.

[13] X. Shi, J. Gao, Q. Lv, H. Cai, F. Wang, R. Ye, and X. Liu, “Calcification in Atherosclerotic Plaque Vulnerability: Friend or Foe?,” *Frontiers in Physiology*, vol. 11, 2 2020.

[14] P. Doradla, K. Otsuka, A. Nadkarni, M. Villiger, A. Karanasos, L. J. Zandvoort, J. Dijkstra, F. Zijlstra, G. v. Soest, J. Daemen, E. Regar, B. E. Bouma, and S. K. Nadkarni, “Biomechanical Stress Profiling of Coronary Atherosclerosis: Identifying a Multifactorial Metric to Evaluate Plaque Rupture Risk,” *JACC: Cardiovascular Imaging*, vol. 13, pp. 804–816, 3 2020.

[15] I. Loftus, *Mechanisms of Vascular Disease: A Reference Book for Vascular Specialists.* Adelaide: University of Adelaide Press, 2011.

[16] J. N. Cameron, O. H. Mehta, M. Michail, J. Chan, S. J. Nicholls, M. R. Bennett, and A. J. Brown, “Exploring the relationship between biomechanical stresses and coronary atherosclerosis,” *Atherosclerosis*, vol. 302, pp. 43–51, 6 2020.

[17] A. Abdollah, *Application of Virtual Fields Method for the mechanical characterization of atherosclerotic plaques.* Delft University of Technology, MSc. Thesis, 6 2022.

[18] A. Çağdaş Akyıldız, *Biomechanical Modeling of Atherosclerotic Plaques for Risk Assessment.* PhD thesis, Erasmus MC: University Medical Center Rotterdam, 10 2013.

[19] C. Noble, K. Carlson, E. Neumann, B. Lewis, D. Dragomir-Daescu, A. Lerman, A. Erdemir, and M. Young, “Ex Vivo Evaluation of IVUS-VH Imaging and the Role of Plaque Structure on Peripheral Artery Disease,” *Medicine in novel technology and devices*, vol. 8, 12 2020.

[20] C. J. Rodriguez, K. Swett, S. K. Agarwal, A. R. Folsom, E. R. Fox, L. R. Loehr, H. Ni, W. D. Rosamond, and P. P. Chang, “Systolic blood pressure levels among adults with hypertension and incident cardiovascular events: the atherosclerosis risk in communities study,” *JAMA internal medicine*, vol. 174, no. 8, pp. 1252–1261, 2014.

[21] S. A. Lee, H. A. Kamimura, and E. E. Konofagou, “Displacement Imaging During Focused Ultrasound Median Nerve Modulation: A Preliminary Study in Human Pain Sensation Mitigation,” *IEEE transactions on ultrasonics, ferroelectrics, and frequency control*, vol. 68, pp. 526–537, 3 2021.

[22] A. J. M. Spencer, *Continuum Mechanics.* Dover Publications, 2004.

[23] C. K. Chai, L. Speelman, C. W. Oomens, and F. P. Baaijens, “Compressive mechanical properties of atherosclerotic plaques—Indentation test to characterise the local anisotropic behaviour,” *Journal of Biomechanics*, vol. 47, pp. 784–792, 3 2014.

[24] A. C. Akyildiz, H. H. G. Hansen, H. A. Nieuwstadt, L. Speelman, C. L. De Korte, A. F. W. Van Der Steen, and F. J. H. Gijsen, “A Framework for Local Mechanical Characterization of Atherosclerotic Plaques: Combination of Ultrasound Displacement Imaging and Inverse Finite Element Analysis,” *Annals of Biomedical Engineering*, vol. 44, pp. 968–979, 4 2016.

[25] M. Bernal, I. Nenadic, M. W. Urban, and J. F. Greenleaf, “Material property estimation for tubes and arteries using ultrasound radiation force and analysis of propagating modes,” *The Journal of the Acoustical Society of America*, vol. 129, pp. 1344–1354, 3 2011.

[26] R. Dwivedi and V. K. Srivastava, *Fundamental Optimization Methods for Machine Learning.* Academic Press, 1 2023.